DESIGN AND OPTIMIZATION OF EFFICIENT WIRELESS POWER
TRANSFER LINKS FOR IMPLANTABLE BIOTELEMETRY SYSTEMS
(Thesis format: Monograph)

by

Shawon Senjuti

Graduate Program in Electrical and Computer Engineering

A thesis submitted in partial fulfillment
of the requirements for the degree of
Master of Engineering Science

The School of Graduate and Postdoctoral Studies
The University of Western Ontario
London, Ontario, Canada

# Abstract

Wireless power transmission is a technique that converts energy from radio frequency (RF) electromagnetic (EM) waves into DC voltage, which has been used here for the purpose of providing a power supply to bio–implantable batteryless sensors. The main constraints of the design are to achieve the minimum power required by the application, by still keeping the implant size small enough for the living subject's body. Resonance–based inductive coupling is a method being actively researched for the use in this type of power transmission, which uses two pairs of inductor coils in the external and implant circuits.

In this work, we have employed the resonance–based inductive coupling technique in order to develop a design and optimization procedure for the inductors. We have designed two systems with different configurations, and have achieved power transfer efficiencies of around 80% at a coil distance of $50mm$ for both systems. We have also optimized the power delivered to the load (implant) and developed a power harvesting unit. Misalignment issues due to the subject's movements have been modeled for calculating the worst–case alignment, and finite element modeling of the inductors has been performed.

**Keywords:** biomedical implants, wireless power transfer, inductive coupling, resonance–based power delivery, power harvesting, coil misalignment, mutual inductance, finite element method.

# Acknowledgments

I would like to express my sincere gratitude to a number of individuals and institutions, whose generous support has led me to this successful endeavor.

Firstly, I would like to thank Dr. Robert Sobot, my supervisor, for guiding me along the research process and graciously supporting me throughout the course of the degree.

My thanks also go to my undergraduate instructors at Queen Mary, University of London for paving my way to becoming an electrical engineer, by enriching my knowledge base with their expertise and experience.

My gratitude goes to the Electrical and Computer Engineering department at The University of Western Ontario for providing the necessary funding, facilities and a suitable work environment. I would like to thank all of my industrial sponsors as well as Ontario Graduate Scholarship (OGS) committee, for partial sponsorship of this degree.

I would also like thank my instructors and my colleagues at the university, for making this an enriching yet enjoyable journey.

Last but not the least, I give thanks to my parents, for everything they have done for my education, my husband Rezwan, for his ongoing support that has made this degree possible, and my son Sameed, for making everything a worthwhile experience.

# Contents

# List of Figures

# List of Tables

# List of Abbreviations, Symbols, and Nomenclature

| | |
|---|---|
| **WPT** | Wireless Power Transfer |
| **ICPT** | Indcutively–Coupled Power Transfer |
| **RF** | Radio Frequency |
| **EM** | Electromagnetic |
| **RFID** | Radio Frequency Identification Device |
| **PTE** | Power Transfer Efficiency |
| **FEM** | Finite Element Method |
| **PSC** | Printed Spiral Coil |
| **IC** | Integrated Circuit |
| **CMOS** | Complementary Metal–Oxide–Semiconductor |
| **SRF** | Self–Resonant Frequency |
| **PCB** | Printed Circuit Board |
| **PDL** | Power Delivered to the Load |
| **SAR** | Specific Absorption Ratio |
| **ESR** | Equivalent Series Resistance |
| **KVL** | Kirchoff's Voltage Law |
| **RMS** | Root–Mean–Square |
| **FDTD** | Finite–Difference Time–Domain |
| **DC** | Direct Current |
| **AC** | Alternating Current |
| **IEEE** | The Institute of Electrical and Electronics Engineers |
| **MPE** | Maximum Permissible Exposure |
| **PEC** | Perfect Electric Conductor |
| **CMT** | Coupled–Mode Theory |
| **RLT** | Reflected Load Theory |

# Chapter 1

# Introduction

Interest for biomedical implantable devices is gaining momentum among both health professionals and researchers since they offer a variety of applications. Examples of applications include automatic drug delivery systems, devices to stimulate specific organs, and monitors to communicate internal vital signs to the outer world. Though all of these devices perform different tasks, one of their common issues is that of power requirements, which is a widely researched area over the past decade.

Genetically engineered laboratory subjects under medical studies are often implanted with microsensors that are connected by transcutaneous wires. This technique guarantees a constant power supply and reliable data transmission of the recorded signals, while its main shortcoming is that it requires the subject to be under anesthesia and, therefore, fails to generate undistorted life–like physiological data of an untethered freely moving subject [2]. In addition, the size of the battery that is used as the power source is a limiting factor for the implant's miniaturization and lifetime, while the battery itself requires periodical surgical replacement with possible adverse consequences on the subject such as infections. Hence, a wireless continuous power delivery system is a more suitable method for providing energy to the implants.

This chapter introduces the topic of the present research work. Section 1.1 provides a comprehensive literature review on similar works till date. Section 1.2 presents the motivation

behind the work and the objectives of the research. Lastly, Section 1.3 describes the organizational layout of this thesis.

## 1.1 Review on Inductive Power Transfer Links

The first demonstration of wireless power transfer (WPT) dates back to 1899, performed by Nikola Tesla in Colorado Springs, Colorado [3]. In his experiment, 200 incandescent lamps were lightened when powered by a base station 26 miles away. A study on wireless monitoring systems was conducted in 1957, where development of endoradiosondes or radio–pills was carried out by [4]. In 1962, a passive echo capsule was also developed for similar purposes (pressure, temperature and pH sensing) by [5]. Since then several research projects have been undertaken in this field, including those that have been clinically evaluated, and whose power requirements vary with device application and can range from tens of *microwatts* to hundreds of *milliwatts* [1], [6].

For implants designed for subjects such as genetically–modified laboratory mice, housing a battery within the implant would not be possible because of size limitations. The researchers in [7] have proposed wireless inductively–coupled power transfer (ICPT) solutions for their telemetry system designed for rats. Their implant uses a rechargeable battery which is charged when the alignment of the coil enables power transfer, and is discharged when it is misaligned. Unfortunately, this approach is not suitable for mice since the battery size would be too large (20mm diameter).

Other energy options would utilize sources from the external environment, such as wind and solar power, as has been implemented in Smart Dust distributed network devices [8]. However, human or animal tissues render these methods unsuitable for biomedical implants. Therefore, a wireless and batteryless approach for power harvesting is achieved with the use of radio frequency (RF) signals through inductive coupling [9]. Additionally, some studies have shown how the same link can also be used for data transfer. Although the primary application for
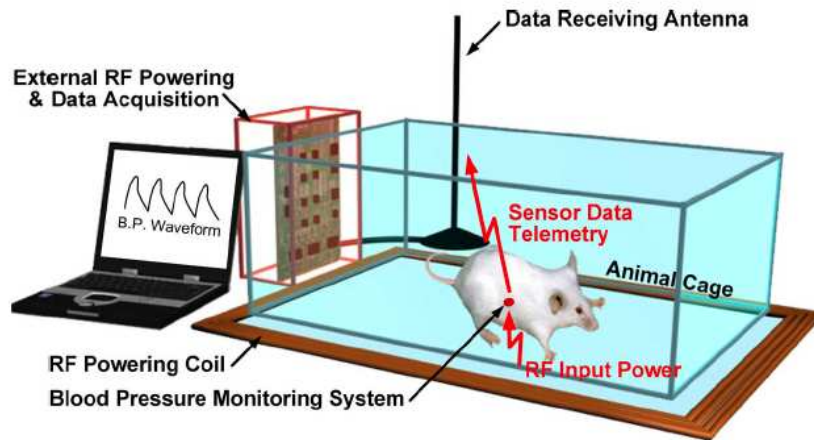
Figure 1.1: General layout of a wireless and batteryless *in vivo* bio–sensing microsystem by Cong *et.al*. [1] ©IEEE 2010

this technique was RF identification (RFID) tags [10], the same principle can be applied to sensor–based wireless biomedical implants [11].

Some latest research endeavors by [1] in 2009 have developed an implant that has a chip area of 2.2x2.2mm$^2$ and weighs 130mg and can be integrated with an artery of the mouse for blood pressure monitoring (Fig. 1.1). The specifications of the chip are ideal for laboratory mice implants given their arterial diameter of about 200um [12]. Since magnetic coupling theory enables efficient power transfer only when the magnetic field is perfectly aligned with the inductor, the challenge is to design a powering system that would work independent of the subject's orientation. Such designs, which are mainly focused on the generation of constant minimum power from the floor of the subject's cage, have been investigated in [13].

Inductive coupling has been the most popular method for wireless power transfer, which requires two coils (primary and secondary coils). The efficiency of power transfer between the coils is a strong function of the coil dimensions and distance between them, which is an unde-sired trend in the case of freely–moving subjects. Therefore, the recent alternative method of resonance–based power delivery has been suggested by [14] in 2007 and is explained through the coupled–mode theory [15]. This multiple–coil based approach is used to decouple adverse
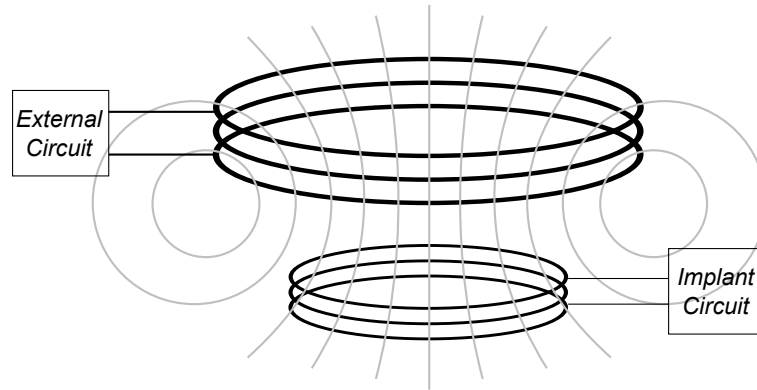
Figure 1.2: Typical setup of inductively coupled coils (with magnetic field shown).

effects of source and load resistance from the coils, and in this way achieve a high quality factor for them. This method is less sensitive to changes in the coil distance and typically employs two pairs of coils: one in the external circuit called driver and primary coils, and the other in the implant itself called secondary and load coils.

Most of the work in this area so far revolves around either static large radii coils for relatively high power transfer applications [14], or printed spiral coils (PSCs) used for low power integrated circuit (IC) implementations [16]. Some latest studies on wireless power transfer to implantable devices based on resonance–based inductive coupling with emphasis on their power transfer link efficiency are presented in [17], [18] and [19].

## 1.2   Motivation and Research Objectives

The aim of this research is to develop a design and optimization system for implementing wireless power transmission to small–size biomedical implants for freely–moving subjects. The system is not application–specific, and thus can be customized and implemented as per application requirements such as size and power.

The analysis is meant to help future discrete–level WPT system designers to directly achieve maximum possible power transfer efficiency for their systems by identifying their design constraints and application requirements. Therefore, the outline of our research objectives can be

defined as follows:

- To be able to completely eliminate the need for batteries in wireless biomedical implants for small–size living subjects, a resonance–based inductively–coupled power transfer system needs to be developed, that is capable of delivering the required power for the implant application (load) with maximum efficiency.

- A step–by–step design process needs to be developed for the modeling of the inductors to be used in the system, which will be able to automatize the development of the entire WPT system, and directly produce the parameter values with the help of specified design constraints and requirements.

- To begin the design procedure, a discrete–component circuit needs to be adopted using the component values achieved from the previous step. Choices have to be made regarding the type of wire to be used for the inductor coils and the operating frequency.

- Optimization of the electrical parameters, which in turn optimizes the inductors' physical specifications, in order to maximize Power Transfer Efficiency (PTE) and output power of the circuit needs to be performed.

- An analytical study on misalignment of the resonating coils need to be performed to identify the worst–case alignment scenarios. The analysis should be verified with measurements and Finite Element Method (FEM) electromagnetic modeling, preferably with the inclusion of real–life animal models.

With the above aims for the research project, a wireless power delivery system with high efficiency along with a comprehensive design flow for modeling and optimization is presented, with a review of previous endeavors by other researchers which have helped set the goal of this research and provided helpful knowledge.

## 1.3   Organization of the Thesis

The research thesis presents the design and optimization procedure for a wireless power transfer link for biomedical implants. It has been organized in the form of chapters that have been described below.

In Chapter 2, the modeling terms involved and optimization of the inductor coils for maximum power transfer efficiency is presented, with the help of analytical results and discussion.

In Chapter 3, the resonance-based wireless power transfer circuit is thoroughly analyzed. Discussions on power requirements, the power harvesting circuit, and typical application systems are also presented.

In Chapter 4, the misalignment of the inductor coils in real–life scenarios is analyzed, with various case descriptions and experimental results.

In Chapter 5, Finite Element Method (FEM) electromagnetic modeling of the inductors is conducted with the help of FEM–based software.

The research work is summarized in Chapter 6. Achievements are listed, and suggestions for future work are presented.

# Chapter 2

# Inductor Modeling and Optimization

This chapter deals with the various modeling parameters required for the design of the inductor coils, such as, inductance, capacitance and resistance of the coils. Analytical models for each of the parameters are presented, which is followed by detailed analysis of the design flow and optimization of the entire resonance–based power–transfer system.

The inductor coil models are based on a multilayer helical structure wound around a plastic base using a special type of wire called the Litz wire. However, the design flow has been generalized to accommodate any inductor type that requires similar design parameters. This can be easily performed by changing the governing equation for the specific parameter.

As opposed to CMOS (Complementary Metal–Oxide–Semiconductor) coils, helical and spiral coils are only able to operate in a moderate frequency range of a few hundred *kilohertz* to a few *megahertz* since they have a larger size and a lower self–resonant frequency (SRF) due to high parasitic capacitance. However, they are able to achieve a higher self–inductance, thus an unconstrained quality factor and a better efficiency profile with respect to a carefully–designed compact and optimized size. We will investigate details of the previous statement in following sections of the thesis.
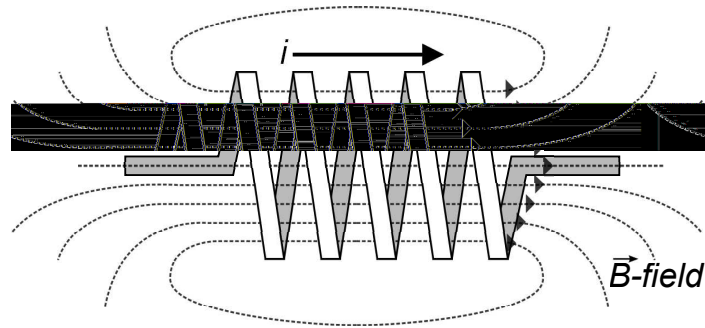
Figure 2.1: Basic inductor showing current and magnetic field.

## 2.1 Overview

An inductor is defined as a passive electrical component with two terminals. In contrast to capacitors, which store energy in their electrical fields, the inductor stores energy in its magnetic field. Typical inductors are made of a wire or other conductive material wound into a coil, in order to amplify the magnetic field.

Inductance can be described using Faraday's law of electromagnetic induction coupled with Lenz's law. The basic definition states that when the current flowing through an inductor changes, a time–varying magnetic field is created inside the coil, and a voltage is induced, which opposes the change in current that created it (Fig. 2.1). Therefore, inductors are classical components used in electronics where current and voltage vary with time, due to the their ability to change the phase of alternating currents.

An inductor can be modeled as an *ideal* inductor, with only an inductance value but no resistance, capacitance, radiation or energy dissipation. However, *real* inductors consist of all of the above unavoidable components, such as resistance (due to resistance of the wire and losses in the core material) and parasitic capacitance (due to the electric field between wire turns which are at slightly different potentials). These behaviors become more pronounced at higher frequencies, and there lies a frequency point where real inductors behave as resonant circuits, becoming self–resonant. Above this frequency the capacitive reactance becomes the dominant part of the impedance of the inductor, and *skin effect* gives rise to very high resistance values, thus deteriorating the quality factor of the inductor.

## 2.2   Modeling Terms

Although different choice of equations are available for modeling inductors, the terms involved in complete modeling for our study and application are analytically described in this section.

### 2.2.1   Mutual Inductance

The mutual inductance of a pair of current–carrying coils is the amount of magnetic flux linkage between them. The mutual inductance is a strong function of the coil geometries and the distance between them. For two non–coaxial and non–parallel filamentary coils, the mutual inductance is [20]

$$M = \frac{\mu_0}{\pi} \sqrt{R_P R_S} \int_0^\pi \frac{(\cos\theta - \frac{d}{R_S}\cos\phi)\Psi(k)}{\sqrt{V^3}} d\phi \tag{2.1}$$

where

$$V = \sqrt{1 - \cos^2\phi \sin^2\theta - 2\frac{d}{R_S}\cos\phi\cos\theta + \frac{d^2}{R_S^2}},$$

$$k^2 = \frac{4\alpha V}{(1 + \alpha V)^2 + \xi^2}, \xi = \beta - \alpha\cos\phi\sin\theta,$$

$$\Psi(k) = \left(\frac{2}{k} - k\right)K(k) - \frac{2}{k}E(k), \alpha = \frac{R_S}{R_P}, \beta = \frac{c}{R_P}.$$

| | |
|---|---|
| $\phi$ | angle of integration at any point of the secondary coil; |
| $R_P$ | radius of the primary coil; |
| $R_S$ | radius of the secondary coil; |
| $c$ | distance between coil centers; |
| $d$ | distance between coil axes; |
| $\theta$ | angle between coil planes; |
| K(k) | complete elliptic integral of the first kind [21]; |
| E(k) | complete elliptic integral of the second kind [21]; |
| $\mu_0 = 4\pi \times 10^{-7}$H/m | magnetic permeability of vacuum. |

The above mutual inductance expression (2.1) assumes that the primary coil radius $R_P$ is larger than the secondary coil radius $R_S$. It is the most general case, for when the angular misalignment $\theta$ or the axial misalignment $d$ is set to zero in the equation (2.1), it takes more simplified forms.

For our case of multilayer helical coils with axial and angular misalignment, we apply the filament method [22] to (2.1) to calculate the mutual inductance of the entire coil, which produces the following equation [20]:

$$
M = \frac{N_1 N_2 \displaystyle\sum_{g=-K}^{g=K} \sum_{h=-N}^{h=N} \sum_{l=-n}^{l=n} \sum_{p=-m}^{p=m} M(g,h,l,p)}{(2S+1)(2N+1)(2m+1)(2n+1)} \tag{2.2}
$$

where

$$
M(g,h,l,p) = \frac{\mu_0}{\pi} \sqrt{R_P(h) R_S(l)} \times \int_0^\pi \frac{[\cos\theta - \frac{y(p)}{R_S(l)}\cos\phi]\Psi(k)}{\sqrt{V^3}} d\phi,
$$

$$
V = \sqrt{1 - \cos^2\phi\sin^2\theta - 2\frac{y(p)}{R_S}\cos\phi\cos\theta + \frac{y^2(p)}{R_S^2}},
$$

$$
k^2 = \frac{4\alpha V}{(1+\alpha V)^2 + \xi^2}, \xi = \beta - \alpha\cos\phi\sin\theta,
$$

$$
\Psi(k) = \left(\frac{2}{k} - k\right)K(k) - \frac{2}{k}E(k), \alpha = \frac{R_S}{R_P(h)}, \beta = \frac{z(g,p)}{R_P(h)},
$$

$$
y(p) = d + \frac{b\sin\theta}{(2m+1)}p; \ p = -m,...,0,...,m
$$

$$
R_P(h) = R_P + \frac{h_P}{(2N+1)}h; \ h = -N,...,0,...,N
$$

$$
R_P = \frac{R_1 + R_2}{2}; \ h_P = R_2 - R_1;
$$

$$
R_S(l) = R_S + \frac{h_S}{(2n+1)}l; \ l = -n,...,0,...,n
$$

$$
R_S = \frac{R_3 + R_4}{2}; \ h_S = R_4 - R_3;
$$

$$
z(g,p) = c + \frac{a}{(2K+1)}g + \frac{b\cos\theta}{(2m+1)}p;
$$

$$
g = -K,...,0,...,K, \ p = -m,...,0,...,m.
$$
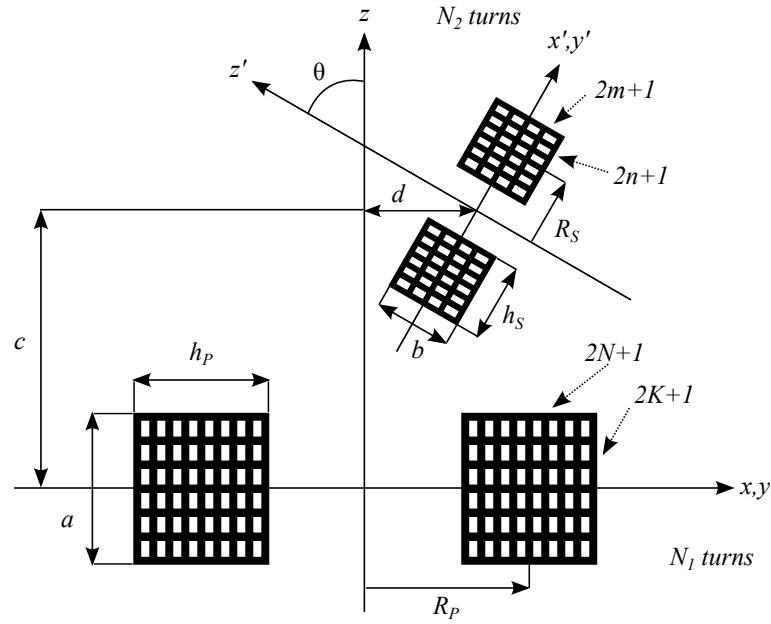
Figure 2.2: Cross–sectional view of two non–coaxial and non–parallel circular coils.

$N_1$    number of turns in primary coil;

$N_2$    number of turns in secondary coil;

$a$    height of the primary coil cross–section;

$b$    height of the secondary coil cross–section;

$h_P$    width of the primary coil cross–section;

$h_S$    width of the secondary coil cross–section;

$R_1$    inner radius of the primary coil of rectangular cross–section;

$R_2$    outer radius of the primary coil of rectangular cross–section;

$R_3$    inner radius of the secondary coil of rectangular cross–section;

$R_4$    outer radius of the secondary coil of rectangular cross–section.

The variables $N$, $K$, $n$ and $m$ in Fig. 2.2 determine the number of cells or subdivisions in the rectangular cross–sectional area of the inductor. Higher values for these variables enhance the accuracy of the result but takes a longer computational time for the integration. Equation (2.2) assumes that centers of all filamentary loops that make up the secondary coil lie in different points away from the primary or secondary coil axes.

## 2.2.2 Self Inductance

The self inductance of a current–carrying coil is the amount of magnetic flux through the cross–sectional area that it encloses. Formulas for finding the self inductance of an inductor coil, such as the planar spiral coil, the helical coil and the printed spiral coil, have been developed, like the ones shown in [16], [23], [24] and [25]. However, this thesis shows how the same equations used for finding the mutual inductance, (2.1) and (2.2), can be modified to produce the self inductance value for each of the coils.

First, we assume that $M$ is equivalent to $L_n$, where $n = 1, 2, 3, 4$, representing the four inductors. Next, we make $a$ and $b$ as half of the actual height of the coil, and $h_P$ and $h_S$ as half of the actual width of the coil. We make $c = a = b$, $d = 0$ and $\theta = 0$, since there is technically no gap and misalignment between the coils (it is the same coil). Finally, we make $R_P = R_S$ and $N_1 = N_2$.

With the above modifications, the same equations (2.1) and (2.2) are applied to find the self inductance values of the four coils. An important term binding the self and mutual inductance values is the coupling coefficient $k$, whose value can range from 0 to 1. When $L_1$ and $L_2$ are the self–inductance of the two coils, $M_{12}$ and $k_{12}$ are related by

$$M_{12} = k_{12} \sqrt{L_1 L_2}$$  (2.3)

## 2.2.3 Parasitic Capacitance and SRF

Parasitic or stray capacitance between turns and layers is a common issue with inductors. It affects the inductor operation by causing self–resonance and limiting the operating frequency of the inductor. Stray capacitance of a single–layered air–cored inductor is modeled analytically in [26], and using numerical methods in [27]. For the case of multilayer multiturn solenoids with $N_a$ layers and $N_t$ turns per layer, stray capacitance is found by [28]

$$C_{self} = \frac{1}{N^2} \left[ C_b(N_t - 1)N_a + C_m \sum_{i=1}^{N_t} (2i - 1)^2 (N_a - 1) \right] \tag{2.4}$$

where $N$ is the total number of turns, $C_b$ is the parasitic capacitance between two nearby turns in the same layer, and $C_m$ is the parasitic capacitance between two different layers. For a tightly wound coil, $C_b$ and $C_m$ are formulated as follows:

$$C_b = \epsilon_0 \epsilon_r \int_0^{\pi/4} \frac{\pi D_i r_0}{\varsigma + \epsilon_r r_0(1 - cos\theta)} d\theta \tag{2.5}$$

$$C_m = \epsilon_0 \epsilon_r \int_0^{\pi/4} \frac{\pi D_i r_0}{\varsigma + \epsilon_r r_0(1 - cos\theta) + 0.5\epsilon_r h} d\theta \tag{2.6}$$

where $D_i$, $r_0$, $\varsigma$, $\epsilon_r$ and $h$ are the average diameter of the coil, wire radius, strand insulation thickness, relative permittivity of strand insulation and separation between each layer respectively [28].

The parasitic capacitance and the self–inductance determine the self–resonant frequency (SRF) of the inductor as

$$f_{self} = \frac{1}{2\pi \sqrt{LC_{self}}} \tag{2.7}$$

### 2.2.4   AC Resistance

At high frequencies, skin and proximity effects increase the effective series resistance (ESR), which decreases the quality factor of the inductor coils. In order to reduce its AC resistance, the coils are commonly made by using multistrand Litz wire [28], [29]. Finite–difference time–domain (FDTD) techniques are used to model AC resistance numerically in [30]. Semi–empirical formulation using finite–element analysis (FEA) is presented in [31]. The AC resistance of these coils, including skin and proximity effects, is found by [32]

$$R_{ac} = \left[ H + K \left( \frac{ND_I}{D_O} \right)^2 \left( \frac{D_I \sqrt{F}}{10.44} \right)^4 \right] \times R_{dc} \tag{2.8}$$
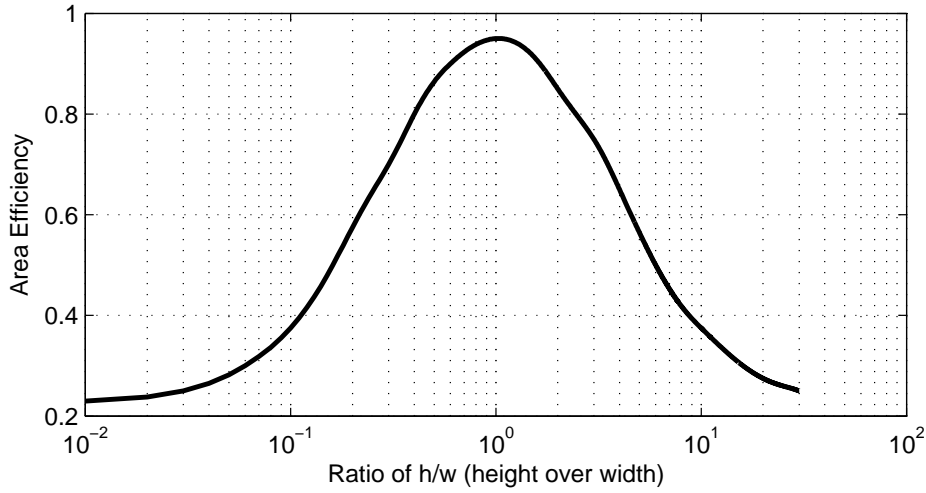
Figure 2.3: Area efficiency of coil ($\eta$) versus coil aspect ratio ($h/w$).

where

$$R_{dc} = \frac{R_S (1.015)^{N_B} (1.025)^{N_C}}{N_S} \qquad (2.9)$$

$H$     resistance ratio of individual strands when isolated (Table 2.1);

$F$     operating frequency in Hz;

$N$     number of strands in the cable;

$D_I$     diameter of the individual strands over the copper in inches;

$D_O$     diameter of the finished cable over the strands in inches;

$K$     constant depending on N ($1.55 < K < 2$);

$R_{dc}$     resistance in Ohms/1000ft.;

$R_S$     maximum DC resistance of the individual strands;

$N_B$     number of bunching operations;

$N_C$     number of cabling operations;

$N_S$     number of individual strands.

There are other equations available to calculate the AC resistance of the coil. The choice of equation depends on the technical data that is given by the manufacturer of the Litz wire used. Another possible set of equations that can be used for similar cases [28] is as follows:

$$R_{ac} = R_{dc}\left(1 + \frac{f^2}{f_h^2}\right) \tag{2.10}$$

where $f_h$ is the frequency at which power dissipation is twice the DC power dissipation and is calculated using the graph in Fig. 2.3 [28]. $R_{dc}$ is given by

$$R_{dc} = \sum_{N_a}^{i=1} \pi N_t D_i R_{ul} \tag{2.11}$$

where $N_a$ is the number of layers, $N_t$ is the number of turns, $D_i$ is the diameter of each layer and $R_{ul}$ is the DC resistance of the unit–length Litz wire.

## 2.2.5  Quality Factor

The total impedance of the inductor after considering the parasitic capacitance and AC resistance is given by [33]

$$Z_t = (j\omega L_{self}) + R_{ac} \parallel \frac{1}{j\omega C_{self}} \tag{2.12}$$

Therefore, the coil can be modeled with an effective inductance $L_{eff}$ and an effective series resistance ESR as

$$L_{eff} = \frac{L_{self}}{(1 - \omega^2 L_{self} C_{self})} \tag{2.13}$$

$$ESR = \frac{R_{ac}}{(1 - \omega^2 L_{self} C_{self})^2} \tag{2.14}$$

An increase in the operating frequency towards the self–resonance frequency (SRF) increases the ESR drastically, and for a frequency higher than the SRF, the coil starts to behave as a capacitor (from (2.13)). The quality factor of the unloaded inductor is given by

$$Q_{unloaded} = \frac{\omega L_{eff}}{ESR} = \frac{2\pi f L_{self}(1 - \frac{f^2}{f_{self}^2})}{R_{dc}(1 - \frac{f^2}{f_h^2})} \tag{2.15}$$

where $f_h$ is the frequency at which power dissipation is twice the DC power dissipation.

Table 2.1: Parameters chart of Litz wire (individual strands)

| Recommended Wire Gauge | Frequency Range | Nominal Diameter over Copper (inch) | Max. DC Resistance (Ohms/m) | Single Strand $R_{ac}/R_{dc}$ "H" |
|---|---|---|---|---|
| 28 AWG | 60 Hz to 1 kHz | 0.0126 | 66.37 | 1.0000 |
| 30 AWG | 1 kHz to 10 kHz | 0.0100 | 105.82 | 1.0000 |
| 33 AWG | 10 kHz to 20 kHz | 0.0071 | 211.70 | 1.0000 |
| 36 AWG | 20 kHz to 50 kHz | 0.0050 | 431.90 | 1.0000 |
| 38 AWG | 50 kHz to 100 kHz | 0.0040 | 681.90 | 1.0000 |
| 40 AWG | 100 kHz to 200 kHz | 0.0031 | 1152.30 | 1.0000 |
| 42 AWG | 200 kHz to 350 kHz | 0.0025 | 1801.0 | 1.0000 |
| 44 AWG | 350 kHz to 850 kHz | 0.0020 | 2873.0 | 1.0003 |
| 46 AWG | 850 kHz to 1.4 MHz | 0.0016 | 4544.0 | 1.0003 |
| 48 AWG | 1.4 MHz to 2.8 MHz | 0.0012 | 7285.0 | 1.0003 |

## 2.3 Litz Wire and Operating Fequency

The term litz wire originates from *Litzendraht*, German for braided/stranded wire or woven wire. It is a type of cable used in electronics to carry alternating current. The wire is designed to reduce the skin effect and proximity effect losses in conductors used at high frequencies. It consists of many thin wire strands, individually insulated and twisted or woven together, following one of several carefully prescribed patterns often involving several levels (groups of twisted wires are twisted together, etc.). This winding pattern equalizes the proportion of the overall length over which each strand is at the outside of the conductor [34].

Analytical models of winding losses in the Litz wire are presented in [35] and [36]. Table 2.1 [32] gives an overview of the parameters used for determining the type of the Litz wire, such as the operating frequency, diameter and resistance. For our purpose of wireless power transfer, the ideal frequency range of operation is from $100kHz$ to $4MHz$, where no biological effects have been reported, in contrast to the extreme–low–frequency band and the microwave band [17]. This restricts our choice of wire from AWG40 to AWG48 (Table 2.1).

## 2.4 Power Transfer Efficiency

The power transfer efficiency (PTE) is a metric for determining the efficiency of the wireless power transfer circuit. It can be simply stated as $P_{out}/P_{in}$, and expressed as a percentage value.

However, it has a direct relationship with the $Q$–factor of the coils and their coupling coefficient $k$. For a four–coil system, PTE is given by [17] [37]

$$\eta = \frac{k_{12}k_{23}k_{34}\sqrt{Q_1 Q_2}\sqrt{Q_2 Q_3}\sqrt{Q_3 Q_4}}{\sqrt{R_1 R_4}[(1 + k_{12}^2 Q_1 Q_2)(1 + k_{34}^2 Q_3 Q_4) + k_{23}^2 Q_2 Q_3]} \tag{2.16}$$

Higher $Q$–factor of the coils and good coupling between them, and lower source and load resistance, yield higher PTE values for the circuit. For resonant–based structures, the low–Q of the driver and load coils (due to the series source resistance of the driver coil, and the load resistance and small size of the load coil) are compensated by the high–Q of the primary and secondary coils, and good coupling between the driver and primary coils ($k_{12}$), and the secondary and load coils ($k_{34}$).

Efficiency does not vary much with respect to the driver coil's $Q$–factor and has a maxima for the load coil's low $Q$–factor [17]. An optimum set of physical and electrical parameters exist for the highest efficiency for each design. This is researched in the following sections.

## 2.5 Design Flow and Optimization

It is a challenging task to determine direct correlations between physical/electrical parameters and performance parameters such as quality factor and power transfer efficiency because of the number of interrelated intermediate parameters in the design process. Changing a certain physical parameter may influence more than one intermediate parameter, all of which in turn affect a particular performance parameter in different ways. Therefore the trend achieved is due to a combination of effects, rendering the direct effect obscure.

This is why a complete design flow and optimization process needs to be developed for the modeling of the inductors. The design flow is based on our design of the multilayer helical inductor. The goal of the design is to improve and optimize power transfer efficiency, for a set of design specifications as per the application system requirements. However, the start of any design is by outlining its constraints, which are given as follows:
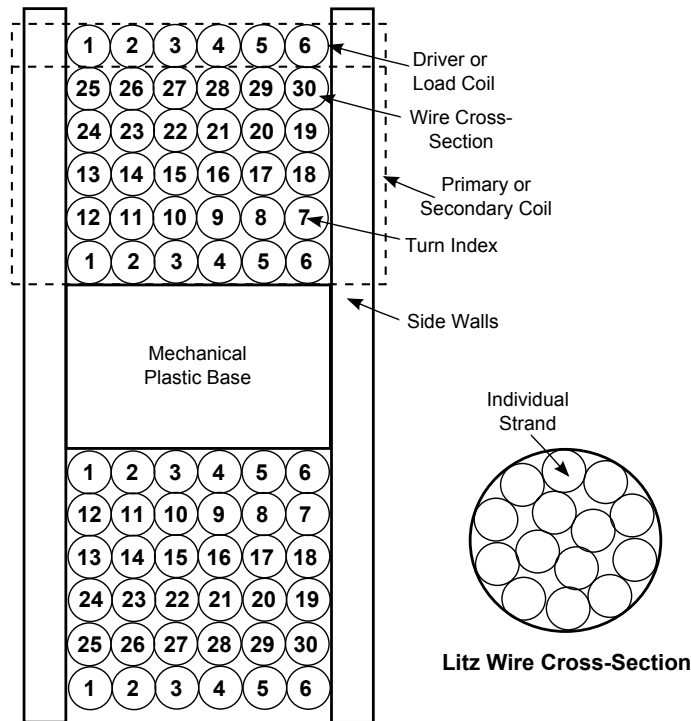
Figure 2.4: Structure of the inductor coils and Litz wire.

• The driver and primary coil pair in the circuit is realized with the help of a plastic base around which the Litz wire is wound (Fig. 2.4). The driver coil is wound above the primary coil concentrically. Similar approach is taken for the secondary and load coils. This is done in order to simplify the structure and maximize the coupling coefficient.

• The radius of the implant coil is chosen as per constraints of the implant size. The focus of our project is to supply power to a biological implant that is meant to be embedded inside the body of a living subject. The current implant design consists of four PCB boards of 15x15$mm^2$ area connected vertically, one of which is the power board that will house the secondary–load inductor pair with approximate diameter of 15$mm$ (Fig. 2.5).

• The radius of the external coil does not have a size constraint theoretically, as it is outside the subject's body. However, in order to maximize the magnetic–field strength, the radius of the external coil is dictated by the typical coil distance (50$mm$) to be covered as per
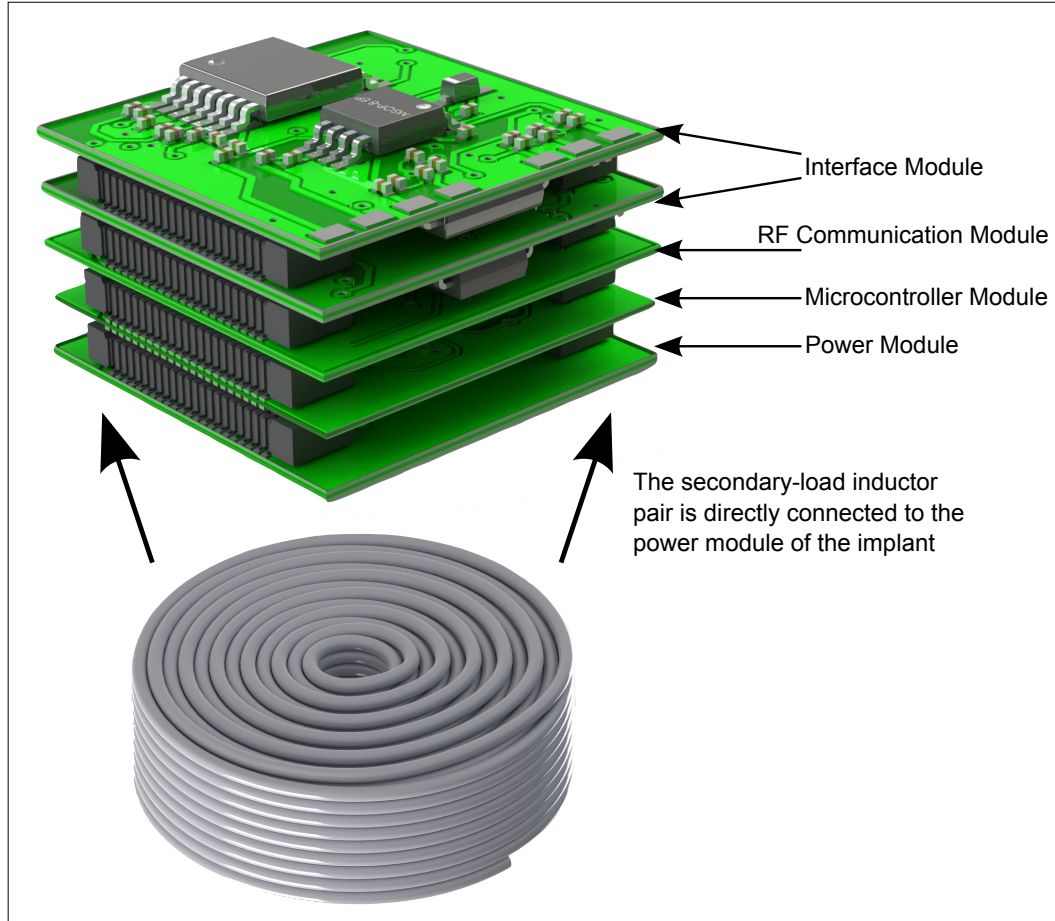
Figure 2.5: The implant PCB boards demonstrating where the inductor is connected.

the relationship *outer diameter = distance* $2 \sqrt{2}$ [38] from the equation [16]

$$H(x, r) = \frac{I.r^2}{2 \sqrt{(r^2 + x^2)^3}} \qquad (2.17)$$

where $H$ is the magnetic–field strength in a single–turn circular coil with radius $r$ at a distance $x$ along the axis, and maximizes when the above relationship is true.

- It is either the chosen wire type that will dictate the operating frequency or a pre–determined operating frequency that will help choose the type of wire. The sequence of these two choices can be decided by the designer.

The type of Litz wire is chosen as per the operating frequency of the circuit. For our project, we want to compare two different systems, each having a different operating frequency
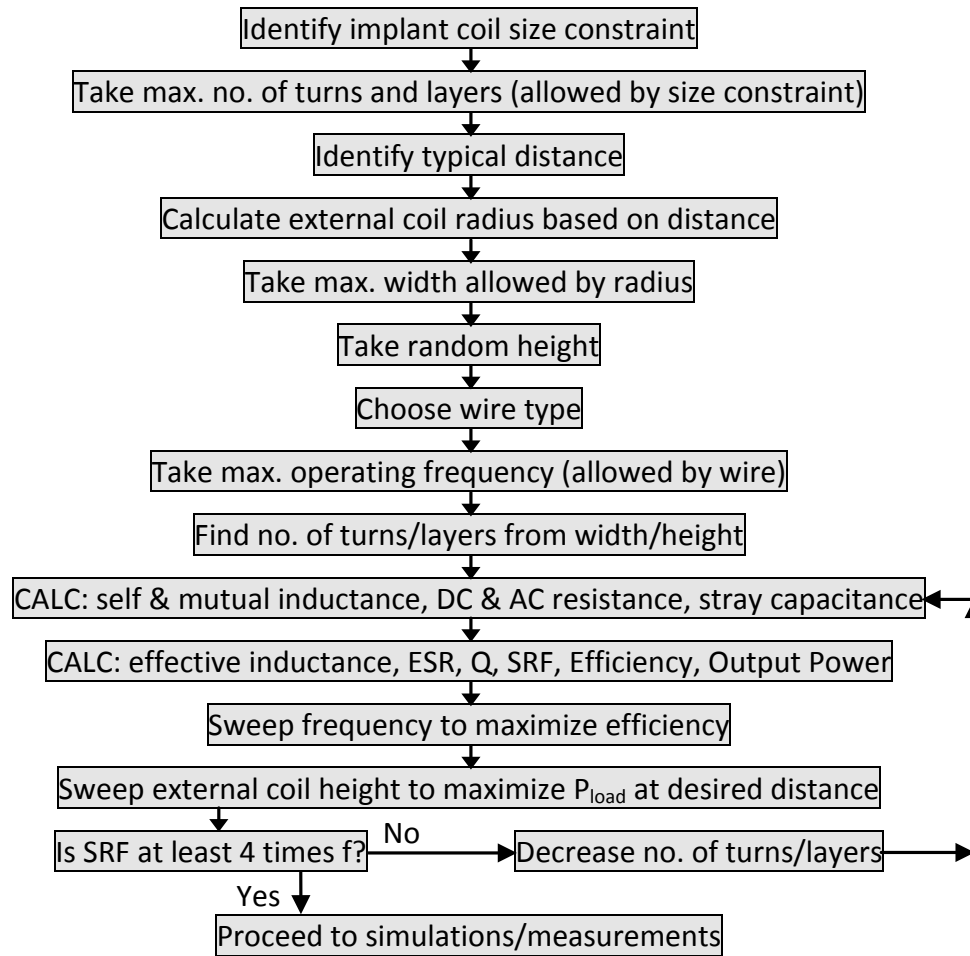
Figure 2.6: Flowchart of the inductor modeling design flow.

and power requirements [39]. Therefore we choose the AWG44 and AWG48 wire types, whose operating frequency range are 350–850kHz and 1.4–2.8MHz respectively [32]. In order for the two systems to be directly comparable and the same dimensions of the implant inductor coil to be re–used, the two wire configurations are selected with approximately the same diameter, 0.48$mm$. Therefore, the AWG44 wire has 40 strands (single strand diameter = 0.05$mm$) and the AWG48 wire has 105 strands (single strand diameter = 0.0305$mm$).

The design flow for the optimization using the modeling terms discussed in Section 2.2 is outlined in the flowchart in Fig. 2.6. As per this design flow and using the design constraints mentioned earlier, we have modeled two different inductor sets, which are called System 1 and System 2. They are described in the following subsections.

## 2.5.1   System 1

We closely follow all the specified design steps of the optimization process in Fig. 2.6 for creating this system of inductors. Firstly, all the design constraints are chosen according to the implant's application criteria. The implant coil diameter is chosen as 15*mm* as mentioned earlier. The Litz wire (40 strand AWG44) is approximately half a millimeter in thickness. Therefore, we make the topmost layer, which is the load coil, have an inner diameter of 14*mm*, thereby making the outermost diameter of the coil very close to, but not above, 15*mm*.

Thereafter, the rest of the inner space is left for the secondary coil winding. Twelve layers can be accommodated, that leaves an small internal 2.24*mm* space to place the base of the plastic spool. We recommend the overall height of the coil not to go over 5*mm* for maintaining compactness of the designed implant. Therefore, the number of turns is 9 for the secondary–load coil pair, which gives a wire–only height of 4.41*mm*.

Since the typical distance between the external and implant coil is taken as 50*mm*, equation (2.17) produces an average external coil radius of 35*mm*, which is chosen. Once again, the driver coil is placed as the outermost layer. The maximum number of layers that can be allowed for the primary coil is 82, which leaves an internal space of 5.22*mm* for the spool base. The number of turns for the driver–primary coil pair is first chosen randomly but later on dictated by the optimization of the power delivered to the load (described in Chapter 3).

The next step is to chose the type of wire, which has been explained previously. This gives us the operating frequency limits. Now we are able to calculate all the electrical parameters of the inductors. This is followed by sweeping of the operating frequency in order to maximize the power transfer efficiency, sweeping of the primary coil height to maximize the actual delivered power, and lastly, checking if the self–resonant frequency of the the coils is within the limit.

This system's physical and electrical specifications are given in Table 2.2. Using the MATLAB® code given in Chapter 4.2, the calculations of the modeling terms are performed for carrying out the optimization procedure. The code also solves for the overall power transfer circuit, which will be discussed in the following chapter.

Table 2.2: Coils' physical and electrical specifications: 40 strand AWG44 ($f$=850$kHz$)

| Coil Type | Outer Dia. (mm) | Inner Dia. (mm) | Turns per Layer | No. of Layers | Height of Base (mm) |
|---|---|---|---|---|---|
| Driver 1 | 136.36 | 134.78 | 2 | 1 | 0.98 |
| Primary 1 | 134.78 | 5.22 | 2 | 82 | 0.98 |
| Secondary 1 | 14 | 2.24 | 9 | 12 | 4.41 |
| Load 1 | 14.98 | 14 | 9 | 1 | 4.41 |
| Coil Type | Inductance (calc.) $L_{self}$ ($\mu H$) | Inductance (sim.) $L_{self}$ ($\mu H$) | Capacitance $C_{self}$ ($fF$) | Self–Resistance $R_{ac}$ ($\Omega$) | $Q$–factor (unloaded) |
| Driver 1 | 1.76 | 1.83 | 40.09 | 0.22 | 43 |
| Primary 1 | 2012 | 2001 | 0.31 | 0.83 | 12946 |
| Secondary 1 | 46.85 | 47.13 | 2.66 | 0.31 | 807 |
| Load 1 | 0.45 | 1.06 | 1.67 | 0.10 | 24 |

From the calculations, the maximum power transfer efficiency is found to be **77.13%** at 50$mm$ coil distance and 850$kHz$ operating frequency, using the optimized parameters. The various parameter trends observed while designing this system and the conclusions drawn from them have been discussed in Section 2.6.

## 2.5.2   System 2

Modeling of this system is similar to that of the previous system. The implant coil dimensions are identical since the implant structure is the same. However, since the Litz wire (105 strand AWG48) and operating frequency are different, the remaining steps of the design flow are also different. The primary coil width and thus the number of turns is restricted to 15, because the self–resonant frequency limit is reached sooner for the higher operating frequency (2.8$MHz$).

Table 2.3: Coils' physical and electrical specifications: 105 strand AWG48 ($f$=2.8$MHz$)

| Coil Type | Outer Dia. (mm) | Inner Dia. (mm) | Turns per Layer | No. of Layers | Height of Base (mm) |
|---|---|---|---|---|---|
| Driver 2 | 83.43 | 81.85 | 2 | 1 | 0.98 |
| Primary 2 | 81.85 | 58.15 | 2 | 15 | 0.98 |
| Secondary 2 | 14 | 2.24 | 9 | 12 | 4.41 |
| Load 2 | 14.98 | 14 | 9 | 1 | 4.41 |
| Coil Type | Inductance (calc.) $L_{self}$ ($\mu H$) | Inductance (sim.) $L_{self}$ ($\mu H$) | Capacitance $C_{self}$ ($fF$) | Self–Resistance $R_{ac}$ ($\Omega$) | $Q$–factor (unloaded) |
| Driver 2 | 0.98 | 0.99 | 24.63 | 0.12 | 144 |
| Primary 2 | 108.03 | 105.22 | 1.78 | 1.21 | 4579 |
| Secondary 2 | 46.85 | 47.13 | 2.66 | 0.18 | 1571 |
| Load 2 | 0.45 | 1.06 | 1.67 | 0.09 | 88 |

|           | radius | width | $w_o$ | height | base |
|-----------|--------|-------|-------|--------|------|
| Primary 1 | 35     | 64.78 | 0.48  | 0.98   | 5.22 |
| Primary 2 | 35     | 11.85 | 0.48  | 0.98   | 5.22 |
| Secondary | 7.5    | 5.88  | 0.48  | 4.41   | 2.24 |
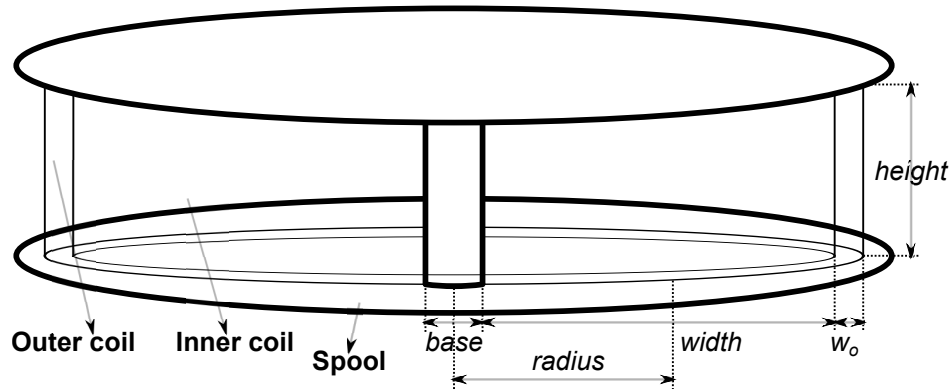
*all dimensions are in millimeters*

Figure 2.7: Physical dimensions of the coils (for both systems).

The maximized power transfer efficiency for this system is **80.66%** at 50*mm* coil distance and 2.8*MHz* operating frequency. This system has the physical and electrical specifications given in Table 2.3.

Figure 2.7 shows the dimensions for all the coils designed for the two systems. As expected, both the systems have peak efficiencies at 50*mm*, which is the distance that they were optimized for by using the external coil diameter. However, this study has proven that fine–tuning of the actual peak output power (or power delivered to the load PDL) for a certain coil distance is possible but requires other parameter choices to be taken into consideration.

## 2.6   Results and Analysis

This section will provide an analysis of the cause–and–effect relationship among the various parameters involved in the optimization process of the power transfer efficiency. Various trends are observed with the help of 2D and 3D graphical plots.

## 2.6.1 Quality Factor of Coils

The Litz wire has been chosen to achieve a low AC resistance and a high quality factor at a specific operating frequency. Litz wires do not offer extremely high frequencies (only up to a couple of $MHz$), but we would not prefer anything higher than $4MHz$ anyway, since human and animal tissue has a lower specific absorption rate (SAR) for low–frequency RF signals compared to the high–frequency signals.
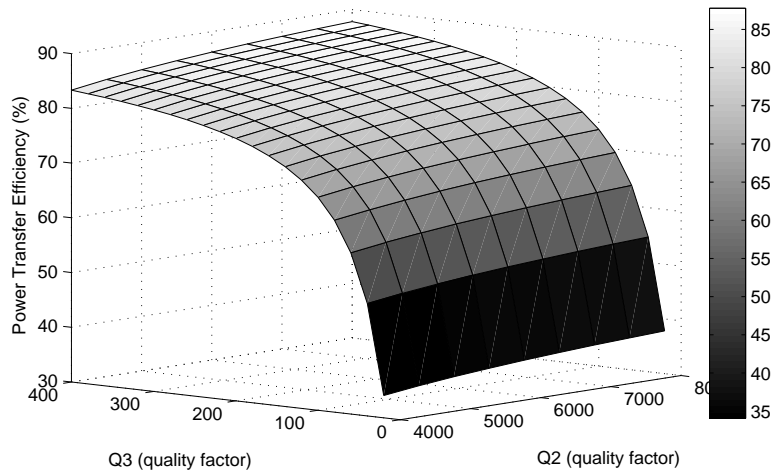


(a)
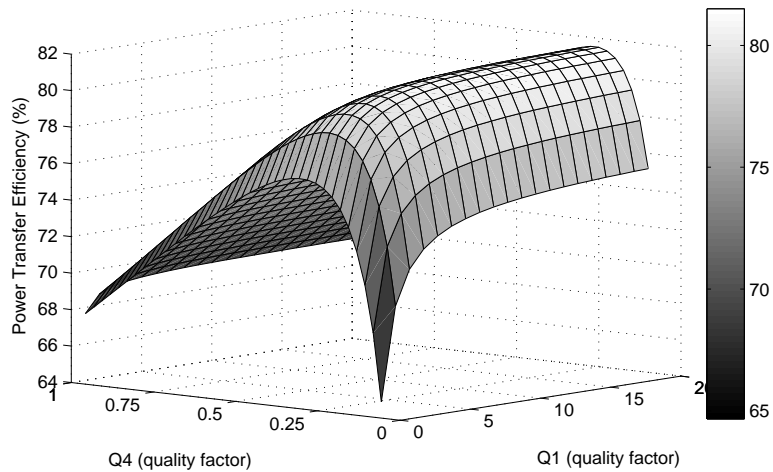


(b)

Figure 2.8: (a) Efficiency versus unloaded quality factors $Q_2$ and $Q_3$ ($Q_1$ = 1.61, $Q_4$ = 0.06). (b) Efficiency versus loaded quality factors $Q_1$ and $Q_4$ ($Q_2$ = 6422, $Q_3$ = 277, $k_{23}$ = 0.01).
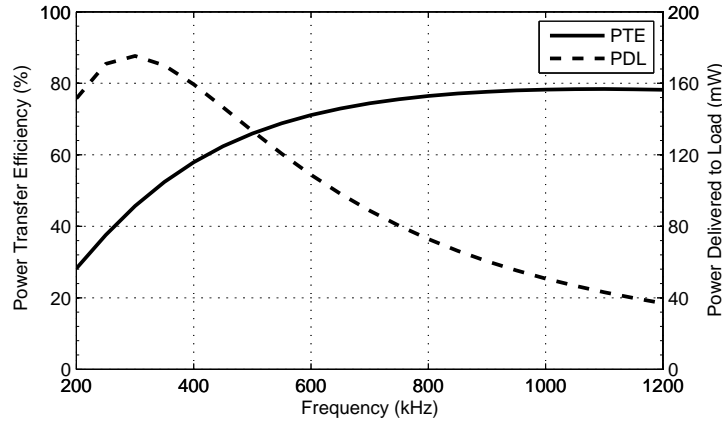
Figure 2.9: Efficiency and output power versus operating frequency (at coil distance=50$mm$).

Also, the small–size implant coil has a small inductance and parasitic capacitance, which means a lower frequency of operation will require a high capacitance value for the external tuning capacitor, thus rendering the capacitance due to tissue effects negligible. Lastly, because of the self–resonant frequency (SRF) constraint of the coil, the operating frequency is needed to be kept low in order to avoid high effective series resistances (ESR). All of the above reasons help us achieve high unloaded quality factors for Coil 2 and 3, as can be observed in Fig. 2.8(a).

The loaded quality factors of the driver and load coils are restricted by the source and load resistances. The $Q$–factor of Coil 4 is very low due to the high load resistance (ranging from 100$\Omega$ to 1$k\Omega$) and small implant size, and the $Q$–factor of Coil 1 is moderate due to the large size of the external coil. However, the efficiency peaks at a certain $Q_4$ value, and remains quite constant with some variation in $Q_1$ values, as can be observed in Fig. 2.8(b).

## 2.6.2   Operating Frequency Variation

The variation in the power transfer efficiency due to changes in operating frequency is not very pronounced in the four–coil system, as opposed to the two–coil system [17]. This is mainly due to the driver coil having a low $Q$–factor due to low inductance, thus having a high bandwidth of operation. Also, the driver coil and high–$Q$ primary coil have a high mutual inductance and coupling coefficient.
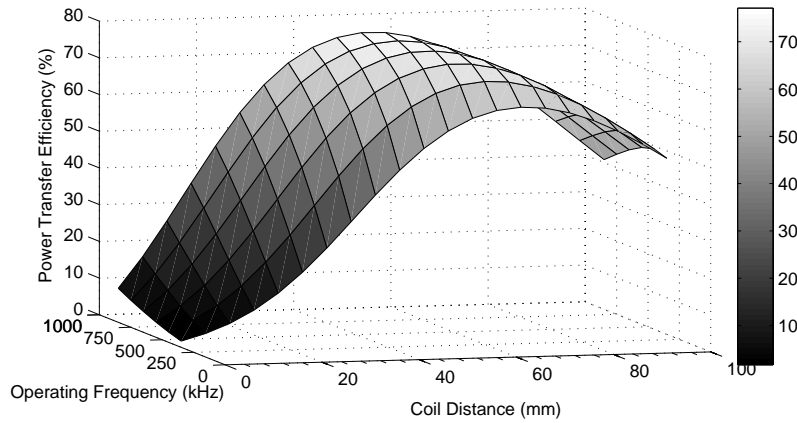
Figure 2.10: Efficiency versus coil distance and operating frequency.
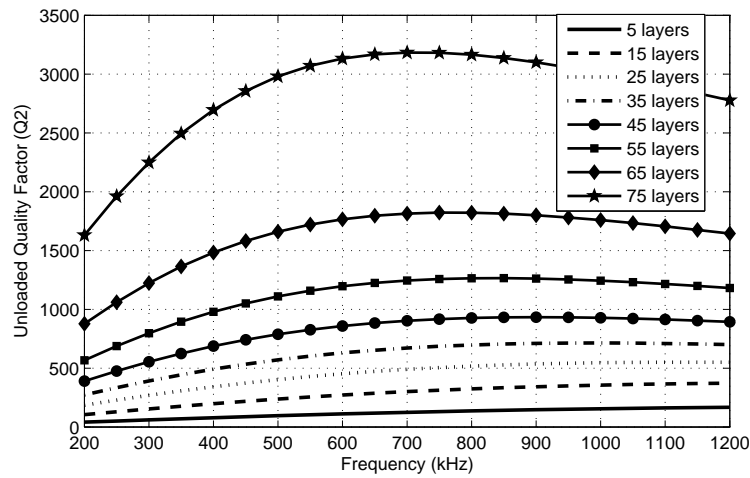


Figure 2.11: Unloaded $Q_2$ versus operating frequency with different number of layers.

Fig. 2.9 and Fig. 2.10 show this phenomenon of relative immunity to operating frequency from $400kHz$ to $1200kHz$. However, the output power (PDL) in Fig. 2.9 decreases with increasing frequency because maximum power can only be delivered to the load when half of the power is dissipated at the source, meaning the efficiency is 50%. This happens at around $300kHz$ in the graph. In Fig. 2.10, the variation of the power transfer efficiency with the coil distance is also observed, with peak efficiency being at $50mm$, as anticipated.

The $Q$–factor of the primary coil does not exhibit much variation for a wide frequency range. In Fig. 2.11, the maximum $Q$–factor achieved is shown as the number of layers of the coil is increased.
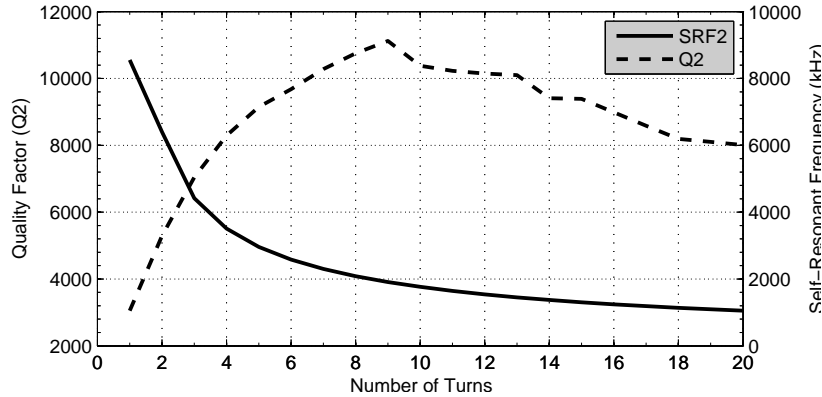
Figure 2.12: $Q_2$ and $SRF_2$ versus number of turns per layer.

## 2.6.3 Choice of Primary Coil Parameters

As mentioned earlier, the primary coil size is the determined by the typical distance where efficiency needs to be maximum, which is why we have chosen a radius of 35$mm$ for a coil distance of 50$mm$ based on (2.17).

For the optimization process to be successful, in System 1, we have used 82 layers for the primary coil with which the self–resonant frequency SRF is still reasonable (6.4$MHz$, which is almost 8 times greater than the operating frequency of 850$kHz$). Going above 82 layers would physically require the coil to have a larger radius, which would in turn change the fine–tuning of the peak efficiency to 50$mm$. For the primary coil in System 1, the width of the plastic base is kept at a minimum of 5.22$mm$, for the spool to be architecturally sound.

For System 2, we have kept the primary coil radius the same because of similar design constraints. However, the number of layers $N_a$ is decreased to 15, because of the SRF constraint. For this system, we have a primary coil SRF of 11.5$MHz$, which is more than 4 times larger than the operating frequency of 2.8$MHz$.

For the choice of the number of turns $N_t$, the determining factor is the output power (PDL) instead of the efficiency (PTE), which will be discussed in the following chapter that discusses the overall power transfer circuit. Fig. 2.12 demonstrates how the $Q$–factor and the SRF of the primary coil vary with $N_t$. As can be observed, the $Q$–factor does not vary much once $N_t$ is
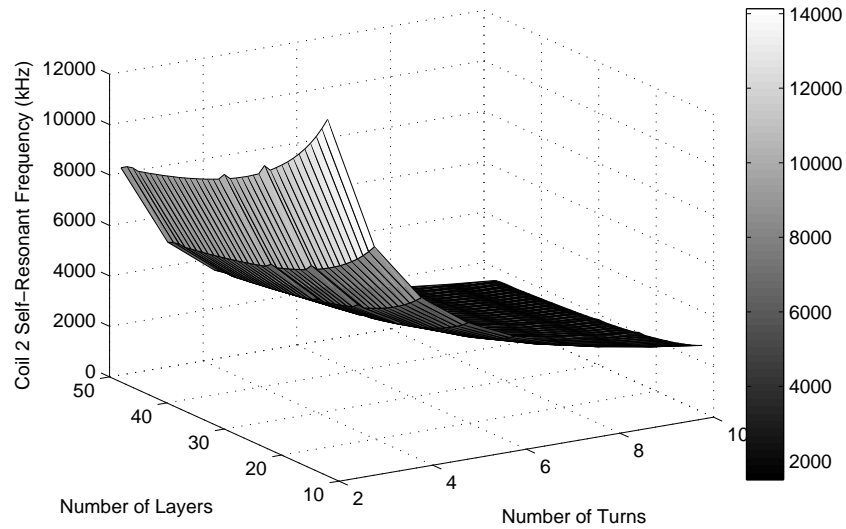
Figure 2.13: Coil 2 SRF versus number of turns and number of layers.

more than 6, which is also true for the SRF. However, both have a steep curve up to 6 turns. The 3D plot in Fig. 2.13 shows the combined effect of change in $N_t$ and $N_a$ on $SRF_2$. It can be observed that an increase in $N_a$ does not drastically reduce the SRF, but rather causes it to have a gradual response.

### 2.6.4   Two–Coil versus Four–Coil Systems

The aim of the resonance–based four–coil system is to avoid the problems observed in the two–coil system, mainly the drastic monotonic decrease of the the power transfer efficiency with an increase in coil distance due to the low coupling coefficient between the primary and secondary coils. Fig. 2.14 clearly demonstrates this. It also shows the pre–determined efficiency peak and the relative immunity of the four–coil PTE for a wide range of coil distances.

## 2.7   Concluding Remarks

This chapter has throughly discussed all the parameters required for successfully modeling a multilayer helical inductor coil for RF power transmission. It has developed a optimization
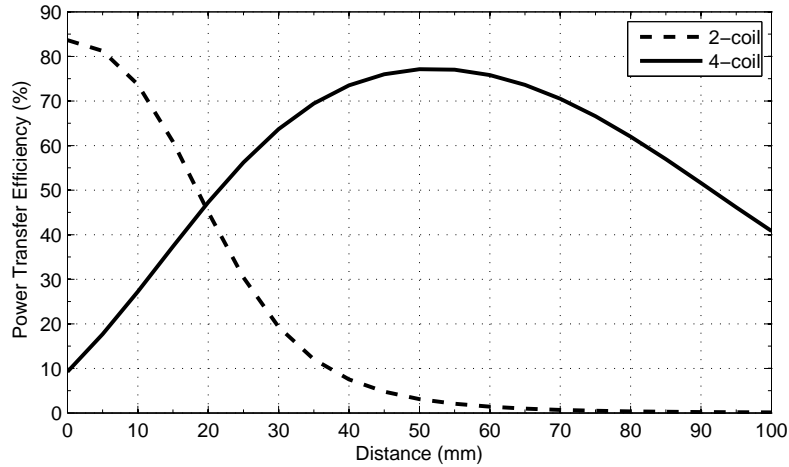
Figure 2.14: PTE versus distance for 2–coil and four–coil systems.

process for maximizing the power transfer efficiency (PTE) in a four–coil system, and demonstrated the various design constraints, choices and trends observed during the design flow.

The two systems discussed have been fully developed with the help of the proposed design and optimization procedure, and their parameters have been tabulated. High efficiency values, 77.13% and 80.66%, have been achieved for both the systems. Graphical plots have been demonstrated in order to clarify how the various parameters are interlinked, and behave under different conditions. The stability of the four–coil system in contrast to its two–coil counterpart has also been established in this chapter.

# Chapter 3

# Power Transfer Circuit

Although coupled–mode theory has been originally used to to describe resonance–based coupling, it can also be transformed into a simple circuit–based model. This chapter explains the physics behind resonance–based power transfer and discusses various details of the system design, such as electrical parameter choices, power harvesting, and application systems. The power transfer circuit is designed using discrete components that are chosen in accordance to the specifications of the modeled inductors in the previous chapter.

## 3.1   Resonance–Based Power Transfer

In 2008, the authors in [40] have investigated and established a non–radiative scheme that can lead to strong coupling between two medium–range distant long–lived oscillatory resonant electromagnetic states with localized slowly–evanescent field patterns, that are practical for efficient medium–range wireless energy transfer.

Although this was the first significant attempt at the resonance–based approach after Nikola Tesla's back in 1914, there have been other ways of wireless energy transfer for several purposes till date. These include the following:

- Radiative modes of omni–directional antennas that work well for information transfer but

are not suitable for energy transfer because of high wastage of energy into free space.

- Directed radiation modes, using lasers or highly–directional antennas, that can be efficiently used for energy transfer even for long distances (distances several times larger than the characteristic size of the transmitting device), but require existence of an uninterruptible line-of-sight and a complicated tracking system in the case of mobile objects.

- Other non–radiative modes such as magnetic induction, but they are restricted to very close–range or very low–power energy transfers.

The resonance–based method is based on the fact that two same–frequency resonant objects tend to couple, while interacting weakly with other off–resonant environmental objects, and even more strongly where the coupling mechanism is mediated through the overlap of the non–radiative near–field of the two objects [40]. This resonant energy–exchange can be modeled by the appropriate analytical framework called coupled–mode theory (CMT) [15], and also by the reflected load theory (RLT) [41].

### 3.1.1   Coupled–Mode Theory

In this system, the field of the system of two resonant objects 1 and 2 is approximated by

$$F(r, t) \approx a_1(t)F_1(r) + a_2(t)F_2(r) \tag{3.1}$$

where $F_{1,2}(r)$ are the eigenmodes of 1 and 2 alone, and then the field amplitudes $a_1(t)$ and $a_2(t)$ can be shown to satisfy, to lowest order [15]:

$$\frac{da_1}{dt} = -i(\omega_1 - i\Gamma_1)a_1 + i\kappa a_2, \ \frac{da_2}{dt} = -i(\omega_2 - i\Gamma_2)a_2 + i\kappa a_1 \tag{3.2}$$

where $\omega_{1,2}$ are the individual eigenfrequencies, $\Gamma_{1,2}$ are the widths due to the objects' intrinsic (absorption, radiation etc.) losses, and $\kappa$ is the coupling coefficient. Equations (3.2) show that at exact resonance ($\omega_1 = \omega_2$ and $\Gamma_1 = \Gamma_2$), the normal modes of the combined system are split

by $2\kappa$; the energy exchange between the two objects takes place in time $\pi/2\kappa$ and is nearly perfect, apart for losses, which are minimal when the coupling rate is much faster than all loss rates ($\kappa \gg \Gamma_{1,2}$). The desired optimal regime $\kappa/\sqrt{\Gamma_1 \Gamma_2} \gg 1$ is called the "strong–coupling" regime, which is set as the figure–of–merit ratio for any wireless energy–transfer system, along with the distance over which this ratio can be achieved.

### 3.1.2  Reflected Load Theory

The authors in [41] have claimed that although CMT is a more physics–based approach and RLT is circuit–based, both the methods produce the same results for ICPT. However, CMT produces relatively simplified equations but works only for very low coupling and high-$Q$ coils. In the RLT method, the resistive load $R_{load}$ is transformed into a reflected load onto the primary loop at resonant frequency. It has been shown that the highest PTE across such inductive links can be achieved when all LC–tanks are tuned at the same resonance frequency [29].

## 3.2  Circuit Specifications

The model for the resonance–based four–coil power transfer system consists of lumped equivalent circuits for the four inductors, referred to as driver, primary, secondary and load coils (also denoted as coils 1 to 4), as shown in Fig. 3.1. In the four–coil system, the high–$Q$ primary and the secondary coils compensate for the low–$Q$ of the source and load coils and the low coupling of the intermediate coils.

The coils are tuned to the operating frequency by varying the tuning capacitance $C_n$ for the given self–inductance as per the equation $\omega = 1/\sqrt{L_n C_n}$. For our example case, a voltage source $E$ of $10.2V$ is used. A source resistance $R_{source}$ of $50\Omega$ and a resistor $R_{sense}$ at $5.5\Omega$ to mimic the source resistance of a power amplifier are used in the first loop, as shown in Fig. 3.2. Lastly, a typical load resistance for implant circuitry $R_{load}$ at $100\Omega$ is included in the last loop of the circuit, apart from the lumped equivalent components of the inductor coils.
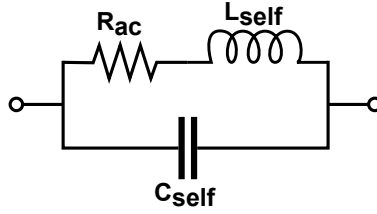
Figure 3.1: Lumped equivalent circuit of the inductor.
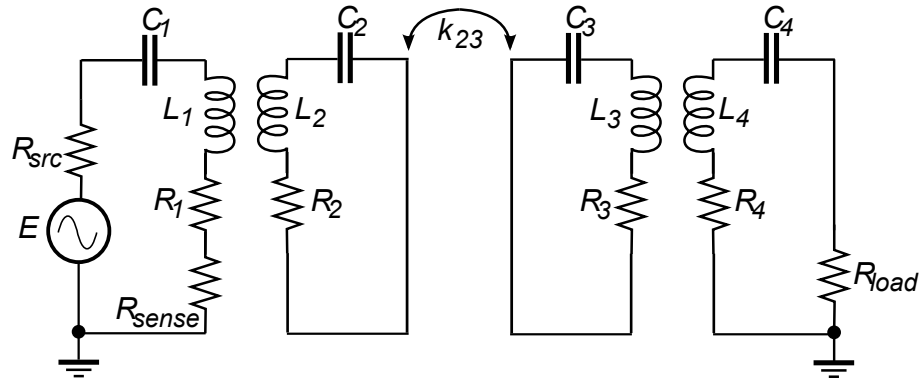


Figure 3.2: Electrical model for the power transfer system.

When circuit theory in the form of Kirchoff's Voltage Law (KVL) is applied to the system, we achieve the following matrix that defines the relationship between voltage applied to the driver coil and current through each coil [17]:

$$
\begin{bmatrix} I_1 \\ I_2 \\ I_3 \\ I_4 \end{bmatrix} = \begin{bmatrix} Z_{11} & Z_{12} & Z_{13} & Z_{14} \\ Z_{21} & Z_{22} & Z_{23} & Z_{24} \\ Z_{31} & Z_{32} & Z_{33} & Z_{34} \\ Z_{41} & Z_{42} & Z_{43} & Z_{44} \end{bmatrix}^{-1} \begin{bmatrix} E \\ 0 \\ 0 \\ 0 \end{bmatrix}
\tag{3.3}
$$

where

$$Z_{mn} = R_n + j\omega L_n + 1/j\omega C_n, \quad \text{for } m = n$$

$$= j\omega M_{mn}, \quad \text{for } m \neq n$$

Coupling coefficients $k_{13}$, $k_{24}$ and $k_{14}$ are neglected due to the small size of the driver and load coils and relatively large distances between the respective coils. Therefore, the matrix elements $Z_{13}$, $Z_{14}$ and $Z_{24}$ are taken as zero so that they do not have an effect on the results.

## 3.3 Input and Output Power

The ratio of the output power over the input power determines the power transfer efficiency. It is an extremely important parameter in wirelessly–powered biological implants because of safety issues and standards regarding tissue exposure to RF electromagnetic radiation [42]. Therefore, maximizing the efficiency will guarantee a relatively high power output at the load even with a relatively low power wave that has to travel through the body.

However, the optimization of the efficiency does not automatically optimize the output power. In cases where we are safely below the exposure limit, and we require a high power delivered to the load (PDL), we can choose to maximize it, even if it at the cost of a lower power transfer efficiency (PTE).

The matrix in (3.3) can be solved for various circuit parameters. For our purposes, we can solve it for the input power and the output power at load resistance $R_{load}$, which produces the following equations:

$$P_{source} = EI_1, \ P_{load} = I_4{}^2 R_{load} \tag{3.4}$$

where $E$ and $R_{load}$ are taken from the circuit's example case as $10.2V$ and $100\Omega$ respectively. Replacing $I_4$, we can achieve the following version of the equation:

$$P_{load} = R_{load} \left[ \frac{j\omega^3 M_{12} M_{23} M_{34} L_2 L_3 \sqrt{L_1 L_4} E}{\sqrt{L_1 L_2} \sqrt{L_2 L_3} \sqrt{L_3 L_4} (M_{12}^2 M_{34}^2 \omega^4 + Z_{11} Z_{22} Z_{33} Z_{44} + \omega^2 (M_{12}^2 Z_{33} Z_{44} + M_{23}^2 Z_{11} Z_{44} + M_{34}^2 Z_{11} Z_{22}))} \right]^2 \tag{3.5}$$

The equation (3.5) determines a direct relationship between the actual power delivered to the load (PDL) and characteristics of the designed inductor such as its self and mutual inductance, stray capacitance and AC resistance. Therefore, we can use this equation in our proposed optimization process directly to maximize the PDL, in a similar approach that was taken to maximize the power transfer efficiency (PTE) in the previous chapter. This is how a PDL versus PTE trade–off can be achieved depending on application requirements.
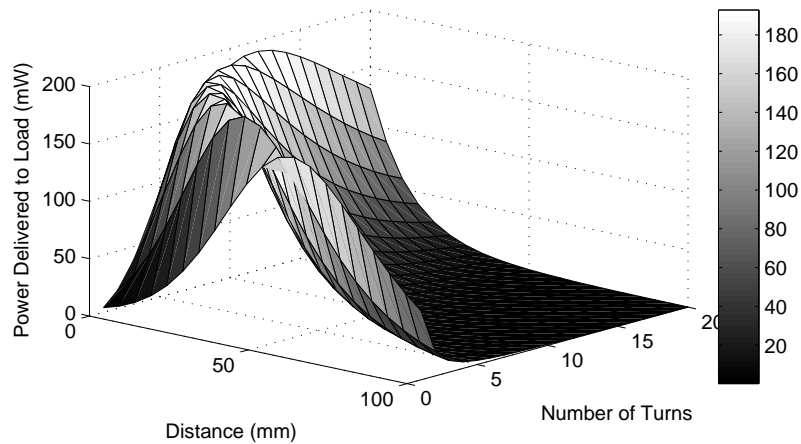
(a)
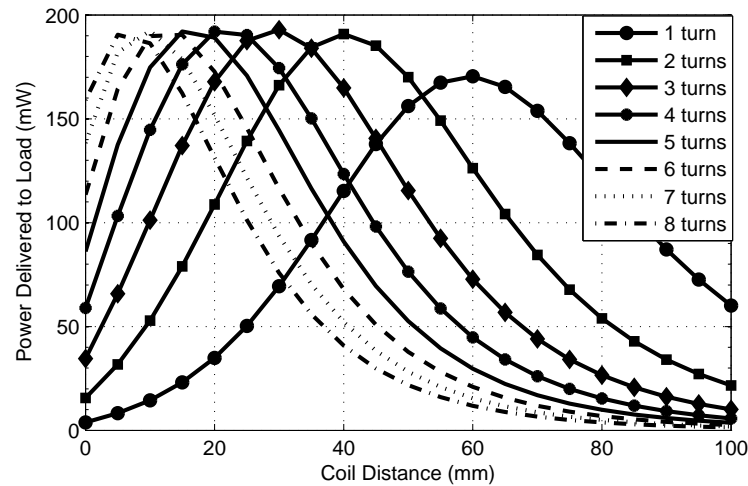


(b)

Figure 3.3: (a) 3D plot for PDL versus coil distance and number of turns. (b) 2D plot for PDL versus coil distance for up to 8 number of turns.

## 3.3.1   Effect of Number of Turns on Peak Power

In contrast to the radius of the external inductor being used to tune the efficiency to a certain coil distance, the PDL tuning is dependent on the height (number of turns) of the external inductor. To demonstrate this, we have conducted a sweep for PDL versus number of turns for a range of coil distances, showed in Fig. 3.3(a) and 3.3(b).

In these graphs, it is observed that the general trend is that the peak PDL will be at a smaller distance as the number of turns increase. The recession of the peak is very distinct
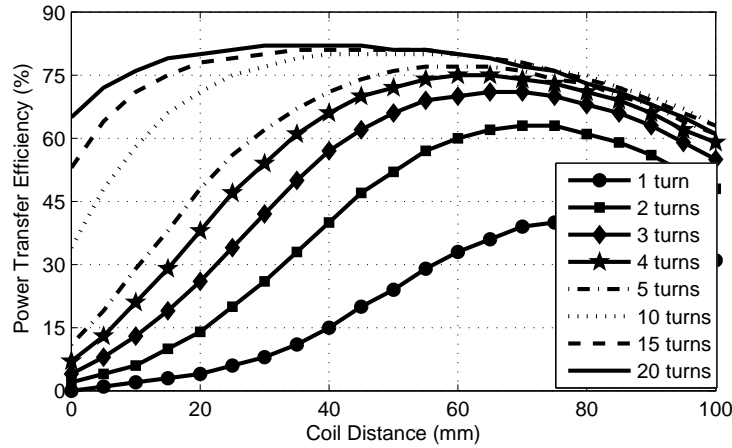
Figure 3.4: PTE versus coil distance for several number of turns.

with increasing number of turns and for our typical coil distance of 50*mm*, we would require about 2 turns only to maximize PDL, which has been incorporated in our two system designs. From Fig. 3.4, it can be observed that the efficiency peak does not vary significantly with increasing number of turns and for a higher number of turns, the efficiency is quite uniform across the range of distances.

## 3.3.2  Effect of Source Resistance

As shown in Fig. 3.5, the source resistance does not have a significant effect on the power transfer efficiency. PTE peaks slightly higher and at a slightly smaller distance with a lower $R_s$.
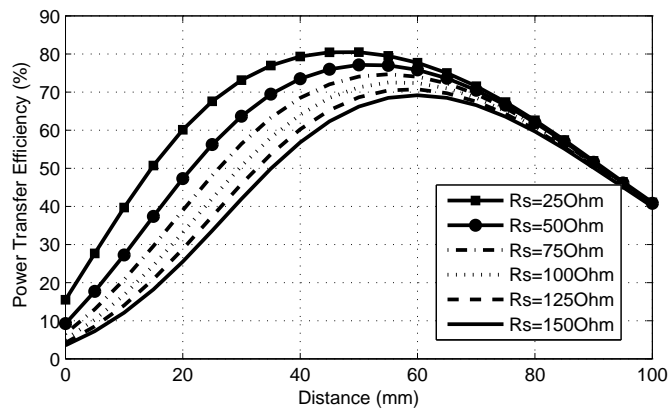


Figure 3.5: PTE versus coil distance for different source resistances.
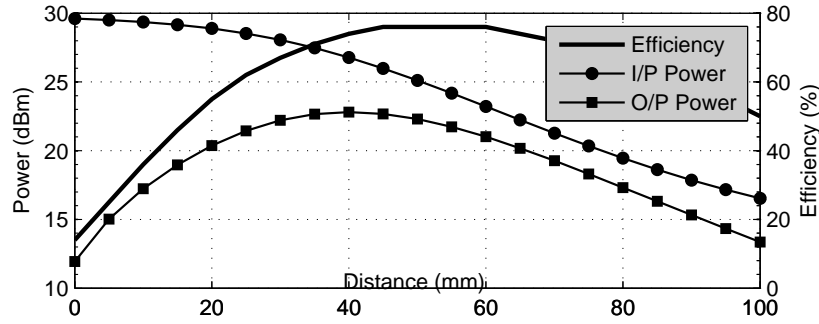
Figure 3.6: Input power, output power, and efficiency of System 1.
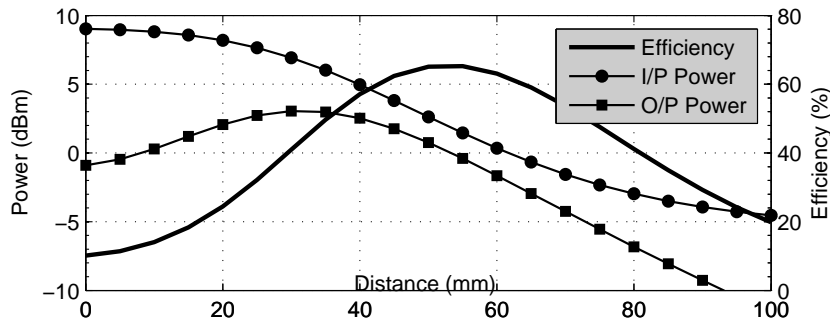


Figure 3.7: Input power, output power, and efficiency of System 2.

### 3.3.3 Results

After performing the optimization of the output power, we have achieved high values for systems 1 and 2 described in Chapter 2, that is shown in Fig. 3.6 and 3.7.

For the coils in System 1, a PDL of $22.3dBm$ has been achieved for $50mm$ coil distance. For the high frequency coils in System 2, a PDL of $0.76dBm$ has been achieved for the same distance. Therefore, our systems have been optimized in a way so that both PTE and PDL are maximized at the same distance between primary and secondary coils.

It is to be noted that for the System 2 circuit, we have chosen an $R_{load}$ value of $1kOhm$ and a voltage source of only $1V$, since it was the requirement for our power harvesting circuit in [43]. Also, for both the systems, the optimized operating frequency was the lower limit of the respective Litz wire, $350kHz$ and $1.4MHz$ respectively. Therefore, it can be concluded that the lower operating frequency limit produces higher PDL values whereas the higher operating frequency limit produces higher PTE values.
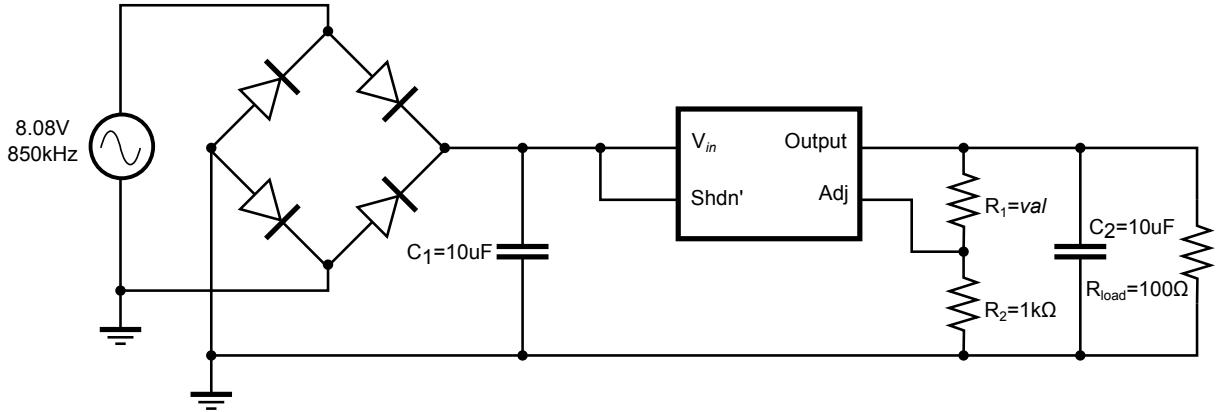
Figure 3.8: Power harvesting unit with rectifier and voltage regulator blocks.

## 3.4   Power Requirements and Harvesting Unit

So far we have only considered the transmission of power from the external circuitry to the implant coil. But the power in this form is not suitable for direct consumption by the implant. Therefore, we have designed a power harvesting circuit that rectifies and regulates the output power into a constant DC form.

Since the power requirements will vary as per the application of the implant, the power harvester circuit has been designed assuming a load resistance of $100\Omega$ for the architecture of System 1 in Chapter 2. This system has a voltage output of $8.08V$ at $850kHz$, which is taken as the input voltage to the power harvesting circuit in Fig. 3.8.

The power harvester is entirely made up of discrete components. The system of diodes is a full–bridge rectifier or AC–to–DC converter. We have used the commonly–used D1N914 diode, which has a high switching speed and low forward voltage drop ($\approx 0.6V$). Any diode with similar rating can be used for the rectifier section. The capacitor $C_1$ is for smoothing the output waveform, and has been calculated using the following relations:

$$V_{dc} = V_{ac} - 2V_D; \; r \approx \frac{V_{dc}}{2fC_1R_{load}} \tag{3.6}$$

where $V_{ac}$ is the AC input, $V_{dc}$ is the DC output, $V_D$ is the forward voltage of the diode and $r$ is the height of the ripple in the output waveform.
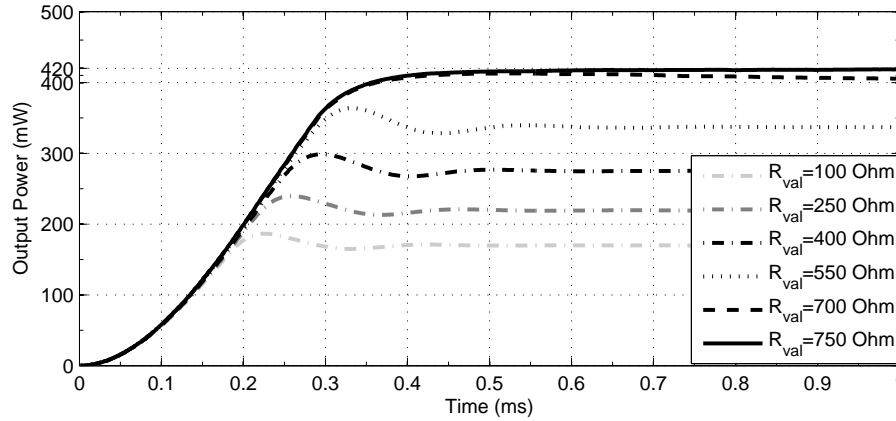
Figure 3.9: Output power versus time for different values of $R_{val}$.

Next we have a voltage regulator or DC–to–DC converter for forcing the output voltage to a certain constant value. For this purpose we have used the LT1121 micropower low dropout regulator with shutdown from Linear Technology. It has a dropout voltage of $0.4V$ and a $150mA$ output current.

Its four pins can be configured as per the requirements. The Shutdown pin has been shorted with the $V_{in}$ since we are not using that feature. The Output and and the Adjust pin have been arranged as a potential divider so that the output voltage at $R_{load}$ can be adjusted by changing the value of $R_1$, thereby changing the $R_1/R_2$ ratio. Without the potential divider, the output voltage would be a constant of $3.75V$ for this regulator.

The graph in Fig. 3.9 shows how the output power varies for different values of $R_1$, and saturates somewhere above $R_1 = 700\Omega$. The maximum power output that can be achieved with this circuit for an $R_1$ of $750\Omega$ or higher is $420mW$, which is suitable for typical biological implant applications.

### 3.4.1   Charge Pump

The charge pump is an optional section to the power harvester unit, which can be added in order to amplify the input voltage to the harvester. For demonstrating the voltage amplification, we have created a charge pump out of discrete components, shown in Fig. 3.10.
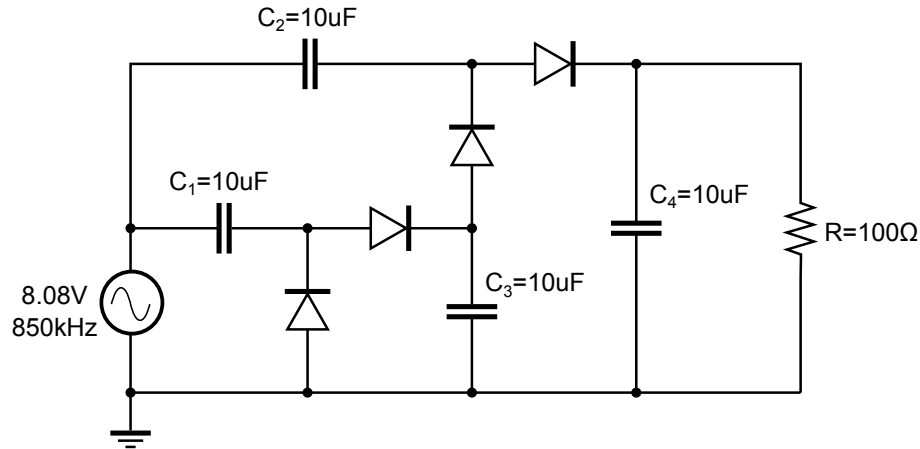
Figure 3.10: The charge pump unit.
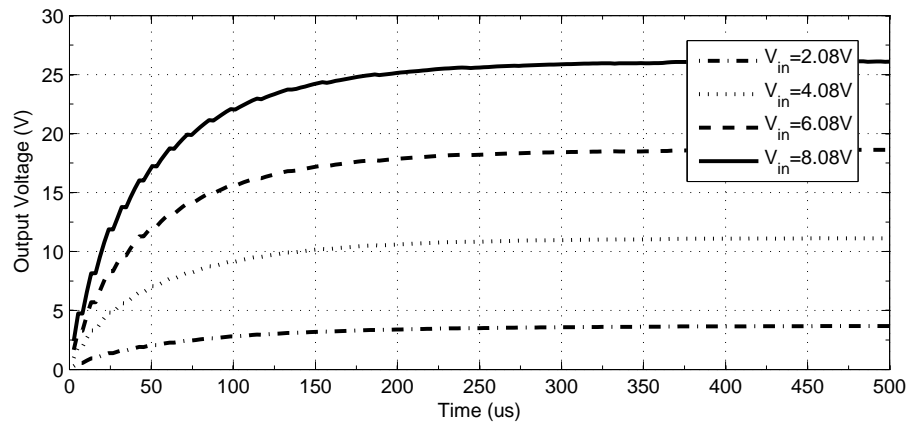


Figure 3.11: Output voltage versus time for different values of $V_{in}$.

This charge pump is a typical variation of the Dickson's charge pump [44]. The input voltage signal is offset by the shunt diode, and the resulting signal is then rectified by the series diode. By stacking a number of charge pump stages, the voltage signal can be multiplied to a much higher value, although adding too many stages also increases the parasitic capacitance of the diodes and the output impedance of the multiplier.

The designed charge pump uses the same voltage input from System 1, and capacitors with a low value of $10uF$ in order to speed up the transient response. It can replace the rectifier unit of the power harvester, if a higher power output is required for the implant application circuitry. Fig. 3.11 shows that for the input voltage of $8.08V$, a voltage of $26V$ is achieved at the output of the charge pump.
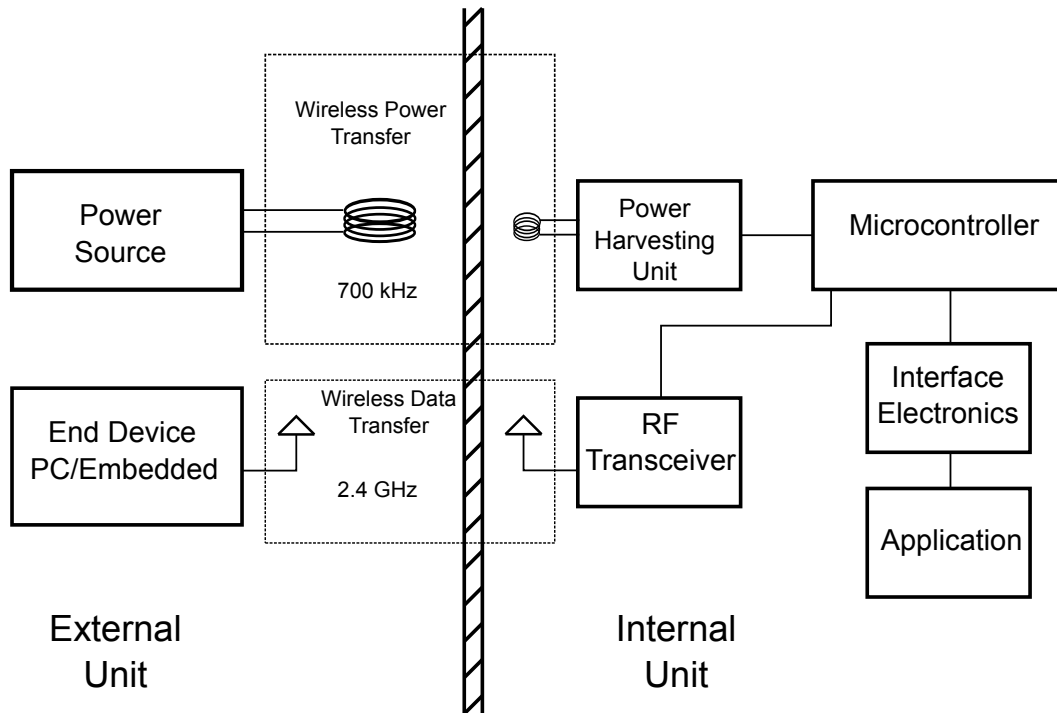
Figure 3.12: Block diagram of overall system: external and internal sub–blocks.

## 3.5   Typical Application Systems

Wireless power delivery can be used for numerous applications of modern autonomous elec-
tronic devices such as cell phones, laptops and household robots. For our project, we are using
it for implantable bio–sensors. This section presents a generic version of such a system, in
order to demonstrate the functions of its various components [38].

The implantable system incorporates the receiver coils designed in the previous chapters.
The overall system is divided into two units: external and internal (Fig. 3.12). The external unit
includes both a power delivery section and an end device. The power delivery section contains
a larger transmitting coil, which is connected to a wired power source, and is designed to allow
for maximum power transfer to the smaller implant coil. The second sub–block is the end
device, which can refer to a computer or a more application–specific embedded system. The
end device is connected wirelessly to the internal unit through a wireless data–link (antenna).

The implantable internal unit is a small application–specific system, designed to capture

bio–sensor data using a custom interface board and communicate it to the end device for further processing. The implantable unit contains three main sub–blocks, a power–harvesting block, a processing and transceiver block, and an application–specific interface block.

The power harvesting section of the internal system comprises of the inductor coil connected to other components to regulate and increase the reliability of the input power to the implant. Apart from the discrete component level power harvesting unit designed in Section 3.4, an Integrated Circuit (IC) level design of the power harvester has also been simulated in CMOS $0.13\mu m$ technology [43]. The design consists of a low–voltage low–power voltage regulator, which includes a charge pump and a temperature insensitive voltage reference.

The internal unit contains a microcontroller and an RF transceiver, that preferably have a low power consumption. The data is transmitted to the end device using Frequency Shift Keying (FSK) modulation at a frequency of 2.45 GHz. This allows the system to work in the Industrial, Scientific and Medical (ISM) band, which allows existing antenna technologies and devices to be used, while reducing developmental time and cost. Any signal processing and data compression is done in the microcontroller before it is sent to the end device.

The interface block of the implant includes bio–sensors that can be used for various applications such as temperature and blood pressure monitoring. The interface electronics are custom to the application in order to reduce the power consumption of the system. Overlapping application areas may use the same or similar electronics, further reducing the size and power consumption of the system. The implantable system is able to be modified to be implanted into lab subjects of various sizes and for different applications. Only modifications to the interface electronics and inductor design are required.

## 3.6   Summary

This chapter implements the inductors designed in this research in the actual implant circuit. It gives a clear overview of the theory behind resonance–based power transfer and how the

coupled–mode theory can be translated into a more circuit–based approach. The circuit speci-fications thoroughly define all the components of the power transfer block of the external and implant circuits, including the lumped equivalents of the four inductors. Circuit theory calcula-tions are used to derive direct relationships between output power and the inductor parameters, so that optimization of output power can be performed by reusing the procedure developed for efficiency optimization.

A novel relationship has been observed between the number of turns of the coil and position of the peak output power in Section 3.3.1. It shows that a greater number of turns shift the peak power to a smaller coil distance. This knowledge will enable future inductor designers to fine–tune their coils as per very specific application requirements. Also, the effect of source resistance on efficiency has been noted.

The results of the optimization procedure have been graphically demonstrated for the two systems described. System 1 has a PDL of $22.3dBm$ and System 2 has a PDL of $0.76dBm$ for their respective specifications. Conclusions have been drawn on the optimal frequency for maximum output power.

In this chapter, a power harvesting unit and a charge pump have been designed to rectify, regulate and amplify the output voltage of the power transfer circuit. A power output of $420mW$ has been achieved with the power harvester and a voltage output of $26V$ has been achieved with the charge pump. Lastly, a typical implant application system has been described with all of its sub–components.

# Chapter 4

# Misalignment Analysis

Most of the studies conducted so far on wirelessly–powered biological implants deal with standard scenarios where the subject would be at a constant distance and/or position from the external circuitry. Some studies, such as [1] and [45] have addressed the issue of misalignment, but have not delved into it as far as the effects and boundaries of misalignment are concerned.

Therefore, in this thesis, we have conducted analysis and calculations on axial and angular misalignment of the primary and secondary coils, with conclusions on the feasibility of the power transfer circuit and allowable worst–case alignments of the two inductors.

## 4.1  Mutual Inductance with Misalignment

### 4.1.1  Overview

An inductive link can be compared to a loosely–coupled transformer for various electromagnetic applications, where the magnetic field generated by the primary coil is partially picked up by the secondary coil, thus enabling wireless power transfer. However, this system needs to be optimized for misalignment tolerance when the implant is meant for living biological subjects. Any misalignment directly affects the mutual inductance, which in turn reduces the overall power transfer efficiency.

Therefore, the formula to find mutual inductance for circular coils in air has to take into consideration both axial and angular misalignments. This research area has a long history of contributions in electrical engineering. A lot of research has been based on the application of Maxwell's formula, Neumann's formula and the Biot–Savart law; as well as the use of analytical or semi-analytical forms expressed over elliptic integrals of the first, second and third kind, Heuman's Lambda function, Bessel functions, and Legendre functions. The problem can also be addressed by using numerical methods, such as the finite element method (FEM) and the boundary element method (BEM).

In this research, we have adopted the approach taken by [46] and [20] that uses the filament method, where coils of rectangular cross–section are replaced by a set of filamentary circular coils. The formulas stated here yield Maxwell's well–known formula for mutual inductance of two circular coils, when the coils are parallel and coaxial. The mutual inductance is calculated using series that converge slowly, and is a good alternative to numerical methods.

### 4.1.2   Cases of Misalignment

The expression for mutual inductance has already been given in Chapter 2 in the form of equations (2.1) and (2.2). They are restated below for the convenience of the reader:

$$M = \frac{\mu_0}{\pi} \sqrt{R_P R_S} \int_0^\pi \frac{(\cos \theta - \frac{d}{R_S} \cos \phi) \Psi(k)}{\sqrt{V^3}} d\phi \tag{2.1}$$

$$M = \frac{N_1 N_2 \sum\limits_{g=-K}^{g=K} \sum\limits_{h=-N}^{h=N} \sum\limits_{l=-n}^{l=n} \sum\limits_{p=-m}^{p=m} M(g, h, l, p)}{(2S + 1)(2N + 1)(2m + 1)(2n + 1)} \tag{2.2}$$

These equations deal with both the axial and angular misalignment cases. However, there are more details about the orientation of the inductors that need to be taken care of while using these equations. This will be the topic of discussion for this subsection, where we will prove the universal nature of (2.1) and (2.2).

The well–known filament method [22] along with equations (2.1) and (2.2) are used for the calculation of the mutual inductance between all pairs of inclined circular coils either with rectangular cross or negligible section. In the calculations, we have to take into account two coils where the axis of the primary coil will be the axis $z$ and the axis of the secondary inclined coil will be the axis $z'$ . In this treatment, it is important to distinguish two cases given below, for which the choice of calculation methods would be different [20]:

- Centers of the filamentary circular coils which replace the secondary inclined coil lie in different points away from the axis of the primary coil.

- All centers of the filamentary circular coils which replace the secondary inclined coil lie in the same point of the axis of the primary coil or they lie in the same point of the axis of the secondary coil.

A detailed analysis of the cases can be found in [20]. For the case where the center of the secondary coil lies in the same axis as that of the primary coil, instead of applying the filament method to (2.1), it is applied to the following equation:

$$M = \frac{\mu_0}{\pi} \sqrt{R_P R_S} \, \cos\theta \int_0^\pi \frac{\Psi(k)}{\sqrt{V^3}} d\phi \qquad (4.1)$$

where

$$V = \sqrt{1 - \cos^2\phi \sin^2\theta},$$

$$k^2 = \frac{4\alpha V}{(1 + \alpha V)^2 + \xi^2}, \xi = \beta - \alpha\cos\phi\sin\theta,$$

$$\Psi(k) = \left(\frac{2}{k} - k\right) K(k) - \frac{2}{k} E(k), \alpha = \frac{R_S}{R_P}, \beta = \frac{c}{R_P}.$$

It can be observed that (4.1) is a simpler form of (2.1), and can be easily achieved by making the axial distance $d = 0$. This implies that the centers of both the coils lie on the same axis. Therefore, for our design, using (2.1) and (2.2) based on only the first case will suffice.

The second case is almost irrelevant for our purpose since it is now only used when the secondary coil is a thin disk coil, as shown in Fig 4.1. However, if we do choose to go with a
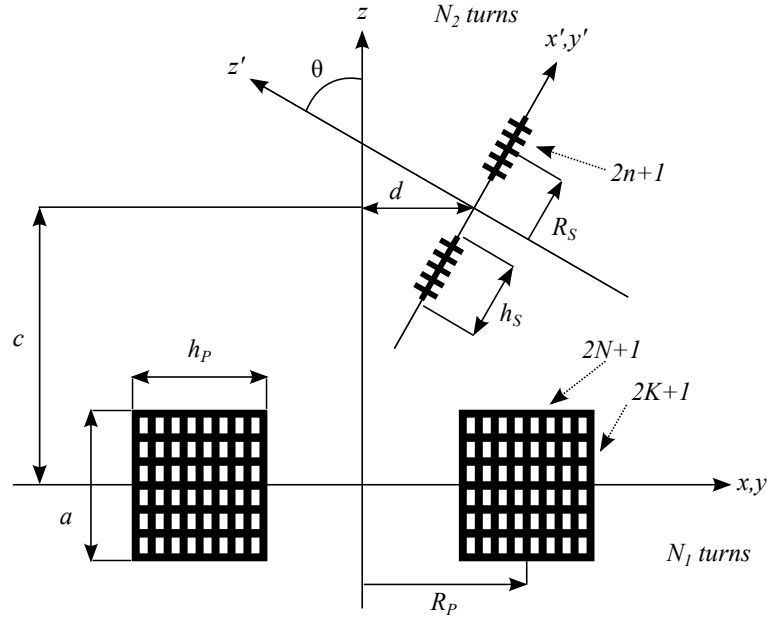
Figure 4.1: Cross–section of two non–coaxial and non–parallel circular coils, where the secondary coil is a thin disk coil, represented by a single filamentary coil.

single–turn secondary coil, we can again use the same set of equations (2.1) and (2.2) for the second case, by suppressing the variable deciding the number of turns ($p = m = 1$) in (2.2) and making $d = 0$ if the coils are coaxial.

Another equation that has been stated in [47] deals with only the non–coaxial case, with the axes of the two coils being parallel:

$$M = \frac{\mu_0}{\pi} \sqrt{R_P R_S} \int_0^\pi \frac{(1 - \frac{d}{R_S}\cos\phi)\Psi(k)}{\sqrt{V^3}} d\phi \qquad (4.2)$$

where

$$V = \sqrt{1 + \frac{d^2}{R_S^2} - 2\frac{d}{R_S}\cos\phi},$$

$$k^2 = \frac{4\alpha V}{(1 + \alpha V)^2 + \beta^2}, \alpha = \frac{R_S}{R_P}, \beta = \frac{c}{R_P},$$

$$\Psi(k) = \left(\frac{2}{k} - k\right)K(k) - \frac{2}{k}E(k).$$

This case too, as shown in Fig. 4.2, can be ignored for our purpose because (2.1) collapses into this form when $\theta = 0$, thus making the term $\cos\theta = 1$.
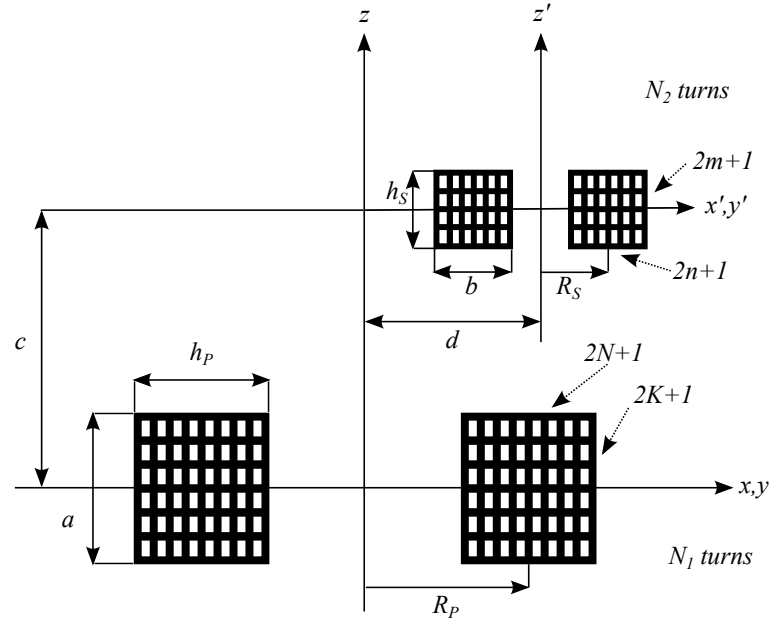
Figure 4.2: Cross–section of two non–coaxial but parallel circular coils.

Therefore, the conclusion on the use of different formulas of mutual inductance for different misalignment cases is that using the general case stated in Chapter 2 is the most efficient method. Other cases can be achieved by assigning appropriate values to the variables involved.

## 4.2 Techniques for Calculation

Essentially, any numerical solver can be used to apply the formulas and produce results. We have used the software MATLAB® for the calculation purposes. A function–based modular approach proved to be the most efficient method for performing the mutual inductance calculations. The flowchart in Fig. 4.3 demonstrates the sequence of these functions starting from the optimization level down to the integration level.

We have chosen the Romberg's Method function (*rombint*) that is predefined in the software to perform the integration given in the expression (2.1). This method is used to estimate definite integrals. The variable *funfcn* describes the integrand of the variable $\phi$ and is called from a separate module, which consists of all the intermediate values such as $V$, $k^2$ and $\Psi(k)$. The domain of integration is from $a$ to $b$, which are set to $0$ and $\pi$ in our case.

```
┌─────────────────────────────────────────┐
│     Function performing PTE/PDL optimization │
└─────────────────────────────────────────┘
     │                    │    ┆    ┆
     ▼                    ▼    ▼    ▼
┌──────────────────┐  ┌──────────────────┐
│ Function handle for │  │   Functions for   │
│ mutual/self inductance │  │  other parameters  │
└──────────────────┘  └──────────────────┘
     │
     ▼
┌──────────────────┐  ┌──────────────────────┐
│ rombint (funfcn, a, b) │─▶│ funfcn: Integrand containing │
│ for Romberg Integration │  │   all intermediate values   │
└──────────────────┘  └──────────────────────┘
```
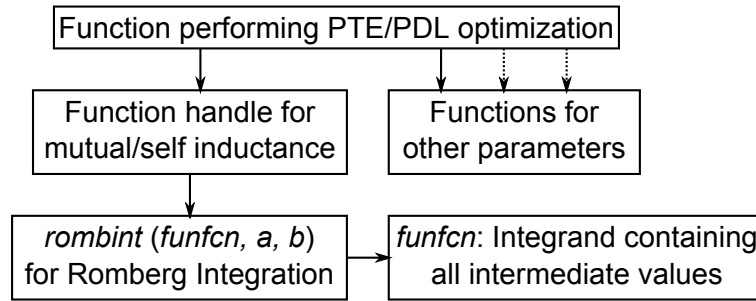
Figure 4.3: Sequence of function calls to perform mutual inductance calculations.

The main code performing the inductance calculations (stored in a file called '*inductance.m*') simply calls the *rombint* function (stored in a file called '*rombint.m*'), declaring its parameters as the integrand *funfcn* (stored in a file called '*integrand.m*' in our case), the lower bound 0 and the upper bound $\pi$. A detailed sequential structure of the MATLAB program is tabulated in Tables 4.1 and 4.2.

## 4.3   Results and Discussion

As stated in the beginning, this chapter is meant to establish strict boundaries on the extent of misalignment between the primary and secondary coils. It needs to be noted that misalignment cases are not considered between the source and primary coils, and the secondary and load coils, since they are wound co–centrically over the same central structure (a plastic base).

The graphs in Fig. 3.6 and 3.7 in the previous chapter have demonstrated input power, output power and efficiency values for different coil distances, calculated with the help of numerical analysis. However, the coils there were considered to be aligned parallelly, with their centers along the same axis.

By using the equations (2.1) and (2.2), and then (2.3), which states the relationship between self and mutual inductance of a coil pair, we are able find the coupling coefficient $k_{23}$ for all types of misalignment cases, which could otherwise only be found empirically through measurements. Once we have the value of $k_{23}$, we can replace it in the **power.m** function in order to find the input and output power of the power transfer circuit.

Table 4.1: Detailed sequence of MATLAB functions used in the optimization process (Part 1)

**MAIN CODE: optimization.m**

- Declaration of all physical properties as global variables such as radius, height, width, distance, number of turns and layers, frequency etc.

- Opening of a text file to save parameter values.

- Code to perform optimization process as per flowchart in Fig. 2.6.

- Calling separate functions for each parameter calculation (described below):

  **1. inductance.m  2. resistance.m  3. self_res_freq.m  4. q_fac_eff.m  5. power.m**

**1. inductance.m**

- Separate codes for all self–inductances ($L_1$, $L_2$, $L_3$, $L_4$) and mutual inductances ($M_{12}$, $M_{34}$, $M_{23}$). $M_{13}$, $M_{24}$, $M_{14}$ neglected (later set to 0) due to size and distance of inductors.

- Calculation of $k_{12}$, $k_{34}$, $k_{23}$ from $L_m$, $L_n$ and $M_{mn}$ values.

- Each inductance calculation involves the following:

  – Assigning values to variables $a$, $b$, $c$, $d$, $R_P$, $R_S$, $h_P$, $h_S$, $N_1$, $N_2$ from the values declared in **optimization.m** for the global variables.

  – Variables $N$, $K$, $n$, $m$ set to 6 (can be set to a higher or lower value to increase or decrease accuracy of calculation as well as speed of code execution.

  – Nested **for** loops run for variables $h$, $l$, $g$, $p$, inside which calculations are performed for $z(g, p)$, $R_P(h)$, $\beta(h, g, p)$, $R_S(l)$, $\alpha(h, l)$ and $M(h, l, g, p)$.

  – For calculating $M(h, l, g, p)$, the **rombint.m** and **integrand.m** functions are called with the command $out = rombint(@integrand, 0, \pi)$.

**1.a) integrand.m**

- Declaration of function $M(h, l, g, p) = integrand(\phi)$.

- Declaration of global variables $R_P(h)$, $\beta(h, g, p)$, $R_S(l)$, $\alpha(h, l)$.

- Performing calculations for $V(l)$, $k^2$, $K(k)$, $E(k)$, $\Psi(k)$ and $M(h, l, g, p)$.

**1.b) rombint.m**

- Predefined function built into MATLAB.

- No changes required.

Table 4.2: Detailed sequence of MATLAB functions used in the optimization process (Part 2)

### 2. resistance.m

- Assigning values to variables and performing resistance (both DC and AC) calculations.

- Equations (2.8) and (2.9) were used for System 1 and equations (2.10) and (2.11) were used for System 2.

- If finding value of $\eta$ to find $f_h$ in (2.10), values are interpolated from the graph given in Fig. 2.3 by using the built–in MATLAB function *spline*.

### 3. self_res_freq.m

- Assigning values to variables and performing calculations for stray capacitance $C_{self}$ as per equations (2.4), (2.5) and (2.6).

- Finding the self–resonant frequency $f_{self}$ from self–inductance $L_{self}$ (from **inductance.m** function) and $C_{self}$ values by using (2.7).

- Using $f_{self}$ to find $L_{eff}$ and $ESR$ values, which are the effective inductance and effective series resistance respectively.

### 4. q_fac_eff.m

- Finding values of $Q_1$, $Q_2$, $Q_3$, $Q_4$ from $L_{eff}$ and $ESR$ values calculated in **self_res_freq.m**. For $Q_1$ and $Q_4$, source and load resistance values are added to ESR in order to make it loaded Q–factor.

- Calculating efficiency from coupling coefficients $k_{mn}$ (from **inductance.m** function) and Q–factor values by using formula in (2.16).

### 5. power.m

- Assigning values to voltage source $E$, $k_{mn}$, and $R_n$, $L_n$, $C_n$ for each inductor coil $n$.

- Nested **for** loops run for $m$ and $n$ to define the KVL matrix in (3.3), in order to find the current through each loop $I_n$.

- Finding values of $P_{in}$, $P_{out}$ and $V_{out}$ by using simple electrical relations.
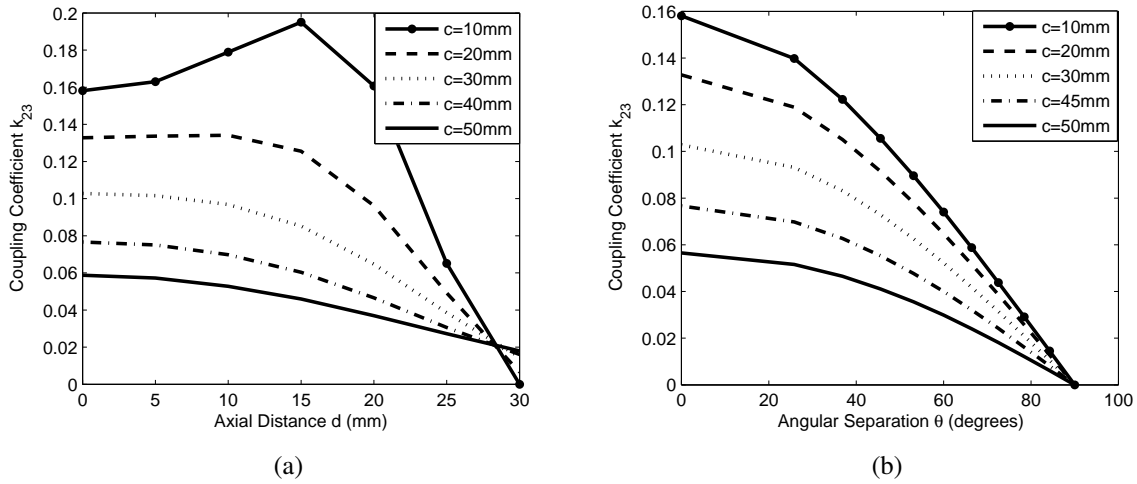
Figure 4.4: (a) Coupling coefficient $k_{23}$ versus angular separation $\theta$ for different coil distances $c$ (axial misalignment $d$ is 0). (b) Coupling coefficient $k_{23}$ versus axial distance $d$ for different coil distances $c$ (angular misalignment $\theta$ is 0).

Therefore, if a minimum output power value can be identified for a system, which must be achievable for the implant to operate properly, it is a straightforward process to find the minimum $k_{23}$ value required. This is how the worst–case values of misalignment can be calculated.

## 4.3.1 Observations and Modeling

For System 1 and System 2, it is observed in the graphs in Fig. 3.6 and 3.7 that the output power maintains a minimum value that is about half of the input power (efficiency = 50%) up to a distance of 75*mm*, after which it deteriorates. The maximum efficiency for both systems is at around 50*mm*, since it is the distance for which the specific external coils (70*mm* average diameter) have been designed. At 75*mm* distance and with perfect alignment between coils, the power delivered to the load $R_{load}$ is 18.3*dBm* for System 1 and -5.55*dBm* for System 2, which are typical adequate levels for the operational purpose of small–size biomedical implants.

Using equations presented in Section 4.1, we have defined the coupling coefficient $k_{23}$ for various coil distances, and axial and angular misalignments, that have produced the graphs in Fig. 4.4 and 4.5. Fig. 4.4 demonstrates the effect of one type of misalignment (either axial or angular), keeping the other constant, for different coil distances.
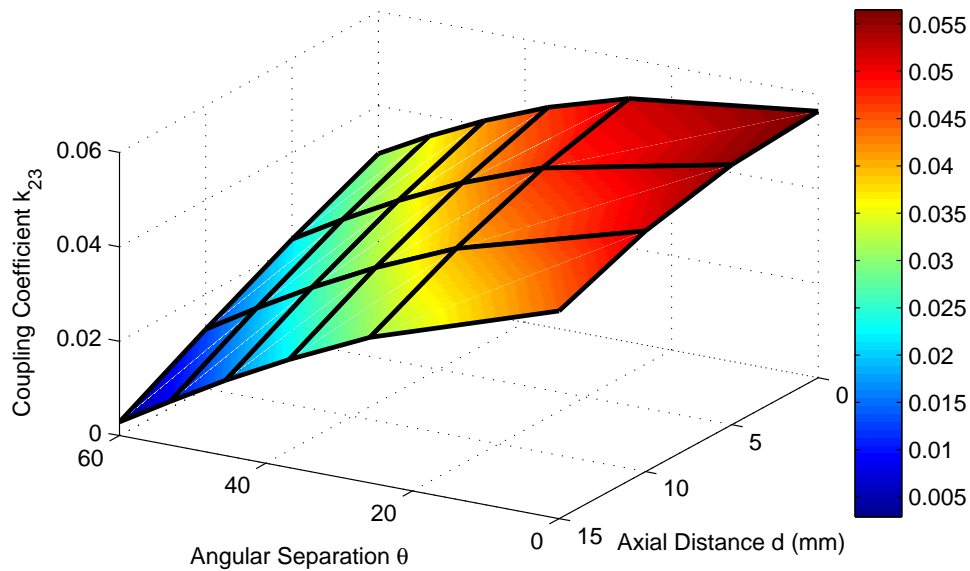
Figure 4.5: Sensitivity analysis of $k_{23}$ with respect to both axial and angular misalignments (c=50*mm*).

The trend, as anticipated, is decreasing coupling coefficient with increasing misalignment, until $k_{23}$ drops to almost zero. However, the function will never reach zero exactly but keep approaching it. A sharp peak is seen in Fig. 4.4(a) for $c = 10mm$ at $d = 15mm$ because at this point the coil distance $c$ is less than the axial misalignment $d$, which causes the magnetic field to be oriented in an unusual pattern.

The 3D graph in Fig. 4.5 shows the simultaneous effects of both types of misalignment, for a fixed distance of 50*mm* between the primary and secondary inductors. The color–coding of this graph can be used to find regions where $k_{23}$ is higher than a specified minimum value.

### 4.3.2    Worst–Case Alignment

Since System 2 has been designed as per the requirements of our integrated circuit in [43], we will consider it as our test–case circuit configuration for analyzing misalignments. This integrated circuit works well in the sub $1mW$ power region, specifically between ($100\mu W$ and $500\mu W$). Therefore, a good power value for us to work with would be $250\mu W$.

At a distance of 75*mm* between the primary and secondary coils, the output power is a little

Set power requirement of implant

Set typical coil distance for setup

Run optimization code for *PTE* and *PDL*

Note $k_{23}$ value for specified output power

Run sensitivity analysis on $k_{23}$ value

Find worst-case alignment
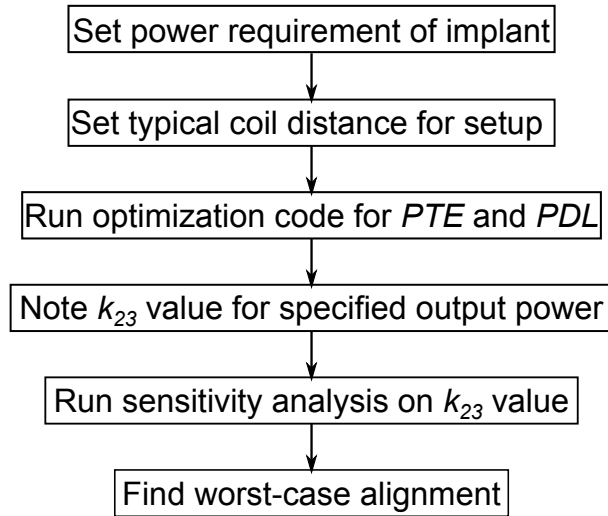
Figure 4.6: Flowchart to find worst–case alignment of primary and secondary coils.

over $250\mu W$ ($279.5\mu W$ precisely). Ideally, similar amounts of power should still be achievable regardless of the inductor orientation. Therefore, an analysis in order to find the worst–case alignment at which $250\mu W$ of power is still deliverable to the $1kOhm$ load has been conducted using the specified equations and graphs. The steps involved are outlined in Fig. 4.6.

To begin with, we note the value of the coupling coefficient $k_{23}$ at the $75mm$ coil distance. Calculating $k_{23}$ from equations (2.1), (2.2) and (2.3), we get a value of 0.032. This implies that $k_{23}$ needs to be at least 0.032 for a minimum of $250\mu W$ of power delivery to the load. From the sensitivity analysis graphs given, it is observed that $k_{23}$ approximates this value when the primary and secondary coils are apart by

- $75mm$ but perfectly aligned (from Fig. 3.6 and 3.7);

- $50mm$ with axial distance of $22.5mm$, but parallel (from Fig. 4.4(a));

- $50mm$ with angular separation of $55°$, but coaxial (from Fig. 4.4(b));

- $50mm$ with axial distance of $10mm$ and angular separation of $37.5°$, or alternatively, with axial distance of $5mm$ and angular separation of $45°$(from Fig. 4.5).

The above–mentioned orientations are the worst–case alignment cases for System 2 to operate successfully with an integrated–circuit biological telemetry system implanted inside
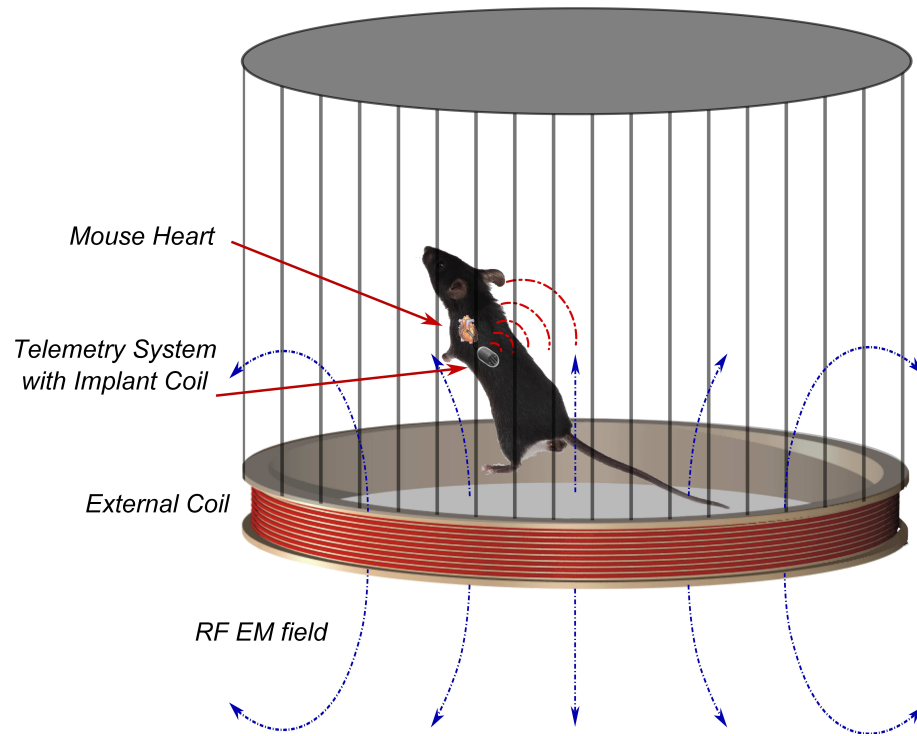
Figure 4.7: Typical subject (mouse) with implanted telemetry system powered by external coil.

a freely–moving subject. Misalignments beyond the orientations considered will reduce the power delivery too much with respect to the specified requirement and the implant circuit will potentially fail to operate.

The best method to physically implement this system is to have the larger coil (driver–primary coil pair) at the bottom of the cage in which the subject is housed, as shown in Fig. 4.7. The walls of the cage should be distanced as such so that the subject is physically unable to cross the axial misalignment boundaries. The angular misalignment boundary is capacious enough to allow for tilted or sleeping positions of the subject.

However, when the implant coil is at 90° angular misalignment, the magnetic flux linkage becomes zero, thus enabling no power transfer. This problem can be avoided with the use of a Helmholtz configuration [48] (with two external coils, each at the top and bottom of the cage), or having more than one implant coil in the form of an array. These implementations will require extensive modifications to be made to the overall system design and are outside the scope of this research work.

## 4.4 Summary

This chapter has dealt with the issue of coil misalignment for the case of freely–moving biological subjects. It has given a thorough description of the different types of possible misalignment cases and what techniques are present for calculating them. It has demonstrated the approach we have taken for calculating coil misalignments for the two designed inductively–coupled power transfer systems.

The series of MATLAB® codes that have been created to implement the overall optimization and modeling of the inductive system, taking care of coil misalignment, has also been given in this chapter. The detailed modular structure of the program will enable future designers to have a better idea regarding implementation procedures.

Sensitivity analysis based on System 2 given in Chapter 2 has been conducted for axial and angular misalignments, as well as the simultaneous effect of both types. Worst–case alignments have been specified for a minimum power supply of $250\mu W$ to the power harvester in [43] using System 2 specifications. It has been shown that if a certain coupling coefficient number is known and needs to be matched, boundaries of misalignment can be calculated for axial, angular and simultaneous cases, by following the series of steps summarized in Fig. 4.6.

# Chapter 5

# Finite Element Method Modeling and Surrounding Environment of Coils

Numerical methods can be implemented in order to verify some of the results we have gathered so far in the previous chapters. This will offer a more solid proof to the analyses conducted and pave the way to manufacturing of the proposed designs. Therefore, this chapter includes the numerical method modeling that has been conducted using the Finite Element Method (FEM) by using commercial software products called COMSOL® and EMPro®. Important electrical parameters of the coils have been evaluated using these software simulations.

This chapter also deals with current standards on the permissible extent of RF radiation and exposure, as well as the effects of the inclusion of external materials including biological matter into the model, since it will be an issue in the real–life operation of the implants.

## 5.1   Introduction to the Finite Element Method

The finite element method (FEM) is a numerical technique for finding approximate solutions of partial differential equations (PDE) and their systems. In simple terms, FEM is a method for dividing up a very complicated problem into small elements that can be solved in relation to each other. Although it has its origin in the field of structural analysis, it is now employed in diverse

areas such as waveguide problems, electric machines, semiconductor devices, microstrips, and absorption of EM radiation by biological bodies [49].

Although the finite difference method (FDM) and the method of moments (MOM) are conceptually simpler and easier to program than the finite element method (FEM), it is a more powerful and versatile numerical technique for handling problems involving *complex geometries* and *inhomogeneous media*. The systematic generality of the method makes it possible to construct general-purpose computer programs for solving a wide range of problems. Consequently, programs developed for a particular discipline have been applied successfully to solve problems in a different field with little or no modification [50].

The finite element analysis of any problem basically involves the following steps:

- **Discretizing** the solution region into a finite number of subregions/subdomains, called *finite elements*;

- **Interpolating** solution for each element;

- **Deriving** governing equations for a typical element;

- **Assembling** of all elements in the solution region;

- **Solving** the system of equations obtained;

- **Post–processing** to generate solutions to required parameters.

Discretization of the continuum involves dividing up the solution region into subdomains, called finite elements. Some typical elements for one–, two–, and three–dimensional problems can be lines, triangles, rectangles, quadrilaterals, tetrahedrons and hexahedrons constituting different number of nodes.

All of the above–mentioned steps are nowadays solved automatically with the help of developed FEM–based software, so the need for hands–on calculations has dramatically reduced. However, the basic principles will enable the reader to visualize the requirements, techniques and application of such a vastly popular numerical method.

## 5.2    COMSOL® 2D Electromagnetic Simulations

This section describes the simulations performed by the software, primarily in order to verify the results for coil resistance, coil self–inductance, and coil mutual inductance with and without misalignments. The version of the COMSOL software used was 4.2a, which contains all the necessary modules for our electromagnetic simulations.

### 5.2.1    Model Setup

A model in COMSOL needs to be set up by following some predefined criteria. The steps involved in setting up the model are given below:

- **Two–Dimensional Model Setup:** The 2D model was set up in the 2D *axisymmetric* dimension. This choice of dimension is very helpful in simplifying complicated 3D geometries and significantly reducing simulation time, since it works with only a cross–section of the geometry and combines the results to 3D at the end.

    The physics added was *Magnetic and Electric Fields (mef)* under the AC/DC module. Lastly, the type of study was chosen as *Frequency Domain* with a frequency of $2.8MHz$.

- **Geometry, Materials and Mesh:** The geometry was defined in *millimeters* as arrays of circles for the primary and secondary helical coils. The boundary was chosen as a semicircle (for sphere in 3D).

    The material assigned to the boundary was Air with *infinite elements*, and to the coil domain was Copper, with slightly modified parameters due to the use of Litz wire. Lastly, the mesh chosen was a *coarser* triangular mesh (Fig. 5.1).

- **Governing Equations:** The coils were assigned with the predefined *Multi-turn Coil Domain* feature of COMSOL. It adds an externally generated current density to the right–hand side of the equation that the Magnetic Fields interface defines. This feature sets the conductivity of the domain to zero because the induced current in the coil windings is
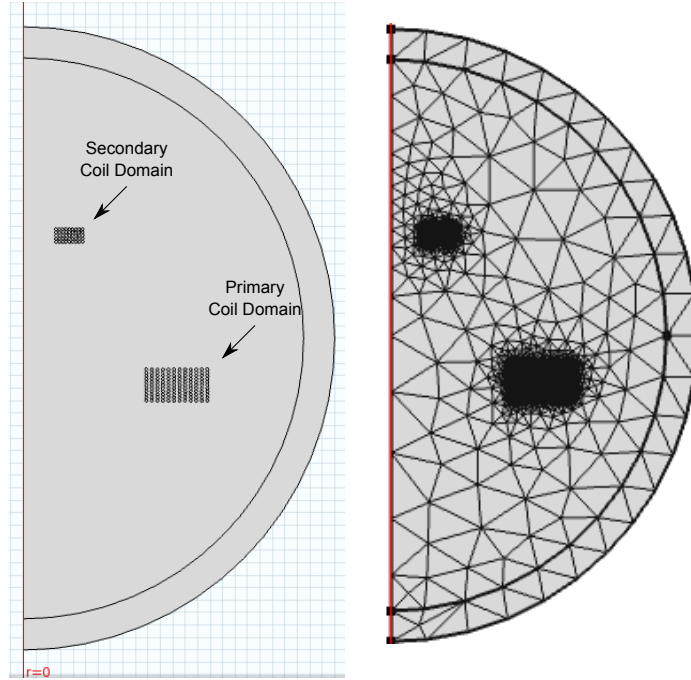
Figure 5.1: 2D coil setup in COMSOL and *coarser* triangular mesh.

handled in a homogenized manner. The external current density can be calculated in different ways, depending on whether a total current or a total voltage is specified. This definition uses the following governing equations:

$$(j\omega\sigma - \omega^2\epsilon_0\epsilon_r)A + \nabla xH - \sigma vxB = J_e \tag{5.1}$$

$$J_e = NI_{coil}/a_{coil} \text{ (for current–driven coil)} \tag{5.2}$$

$$R_{coil} = A\int NL/\sigma_{coil}a_{coil}A \tag{5.3}$$

$$L_{coil} = 2W_m/I^2 \tag{5.4}$$

$$M_{ij} = \Phi_{ij}/I_j = (j/\omega)(V_{induced,ij}/I_j) \tag{5.5}$$

The terms in the above equations follow basic electromagnetic notations. The primary coil domain was assigned with an excitation of $1A$, while the secondary coil domain was set to zero. This was done in order to calculate the induced voltage in the secondary coil.
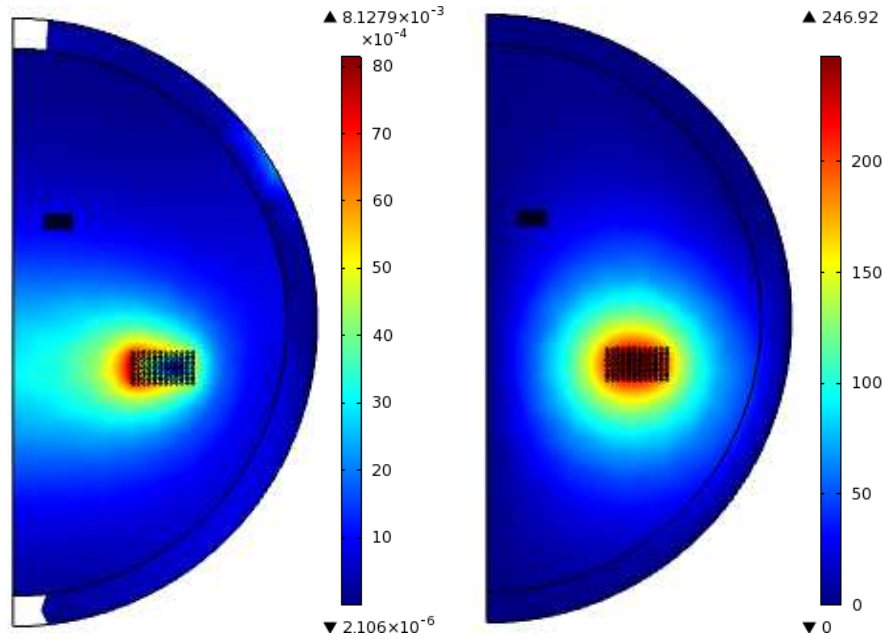
Figure 5.2: Magnetic flux density (normal) and electric field (normal).

## 5.2.2   Simulation Results

The model was simulated with the given setup and specifications, and 2D plots were generated for the magnetic flux density and the electric field, as shown in Fig. 5.2. From the figure, it is evident that both the magnetic flux density and the electric potential is maximum around the primary coil domain, since it has been excited with a current of 1$A$. However, these parameters are not zero around the secondary coil, because of the magnetic flux linkage that causes some amounts of induced voltage in it.

Results for other parameters were also found with the help of COMSOL's built–in functions, such as self–inductance, resistance and mutual inductance of the coils. Table 5.1 shows a comparison and error calculation between the values that were calculated in Chapter 2 for System 2 and the values that were obtained from the COMSOL simulations.

All of the simulation results were within a very close error range of the results calculated using the equations. The maximum error percentage was 5.6%, which was mostly due to approximations in formula and use of a coarser mesh (trade–off between accuracy and run time). Therefore, the EM model in COMSOL has successfully validated the theoretical results.

Table 5.1: Comparison between theoretically calculated and FEM simulated parameter values

| Coil Type | Inductance (calc.) $L_{self}$ ($\mu H$) | Inductance (sim.) $L_{self}$ ($\mu H$) | Error (%) | Resistance (calc.) $R_{ac}$ ($\Omega$) | Resistance (sim.) $R_{ac}$ ($\Omega$) | Error (%) |
|---|---|---|---|---|---|---|
| Primary | 108.03 | 105.22 | 2.6 | 1.78 | 1.88 | 5.6 |
| Secondary | 46.85 | 47.13 | 0.6 | 2.66 | 2.53 | 4.9 |

| Mutual Inductance (calc.) $M_{23}$ ($\mu H$) | Mutual Inductance (sim.) $M_{23}$ ($\mu H$) | Error (%) |
|---|---|---|
| 0.55 | 0.54 | 1.8 |
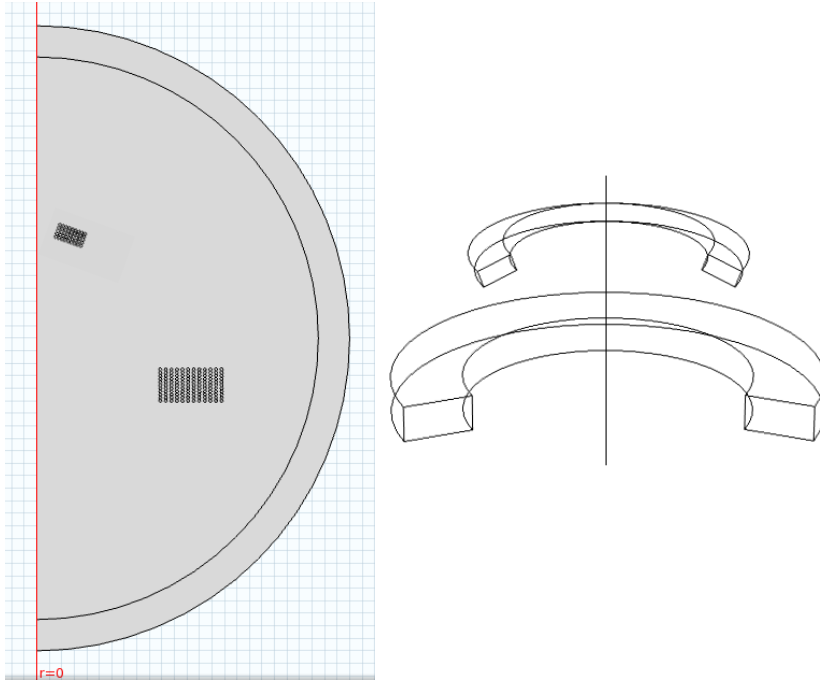


Figure 5.3: Coil setup with the secondary coil being misaligned, and its 3D rendition (view at 225° revolution).

### 5.2.3  Shortcomings of the *2D Axisymmetric*

It appears that the 2D axisymmetric model can be changed for misalignment analyses by axially shifting and tilting the secondary coil cross–section, as shown in Fig. 5.3. However, doing this will not give out correct results, because the model then no longer remains *axisymmetric*.

If the cross–section shown in the figure is revolved by 360° to generate its 3D rendition, it will not generate the correct 3D misaligned secondary coil, but the geometry shown beside the cross–section instead. Therefore, we are required to perform actual 3D simulations for misalignment analysis, as given in the next section.
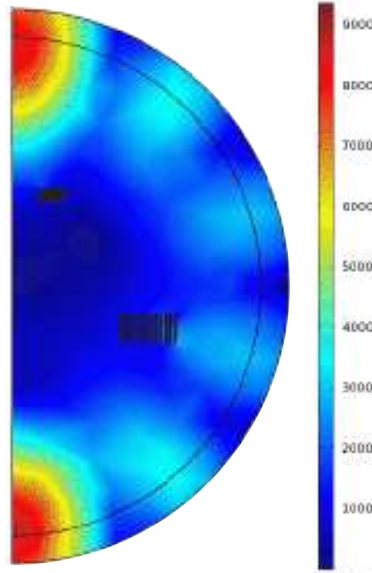
Figure 5.4: Electric field (normal) at 12.80$MHz$ showing noise.

## 5.2.4   Eigenfrequency

Eigenfrequency can be defined as one of the resonant frequencies of an oscillatory system. Increasing the primary coil size increases the parasitic capacitance between its turns and layers. To obtain a high Q–factor at a relatively lower frequency, the inductance of the primary coil, and therefore its size, should be large. This results in a significant effect of parasitic capacitance on its self–resonant frequency or eigenfrequency.

To reduce the parasitic capacitance between the turns and layers, a low dielectric insulating material is usually inserted between the coil layers. As a rule of thumb, the thickness of the dielectric layer should be varied until the eigenfrequency is 3–4 times higher than the frequency of operation so that its effects can be reduced in the coil's overall Q–factor.

Therefore, the last study of the 2D design that was conducted was for the eigenfrequency of the entire coil domain. Through simulations, the eigenfrequencies that were found (in $MHz$) are 8.58, 9.67, 10.72, 11.26, 11.76, 11.86, 12.21, 12.80, 13.08 and 13.13. The lowest eigenfrequency at 8.58$MHz$ is the fundamental one, which is more than three times higher than the system's operating frequency of 2.8$MHz$. Fig. 5.4 shows how the model behaves due to the effect of self–resonance (noise) at a higher operating frequency.

## 5.3   COMSOL® 3D Electromagnetic Simulations

Although the 2D axisymmetric model gives accurate values for a number of parameters, a 3D model was set up as a next step in order to simulate results not possible to achieve through the previous approach. For the 3D simulations, the model was changed to 3 layers and 3 turns for the primary coil, and 1 layer and 3 turns for the secondary coil. This was done because 3D models in general have a much longer simulation time.

### 5.3.1   Model Setup

The steps involved in setting up the 3D model are given below:

- **Three–Dimensional Model Setup:** The model was set up in the 3D dimension. Two physics were added from the AC/DC module, *Magnetic and Electric Fields (mef)* and *Magnetic Fields (mf)*. Lastly, the type of study was chosen as *Stationary*.

- **Geometry, Materials and Mesh:** The geometry was defined in *millimeters* as helices. The primary coil was a combination of three separate 3–turn helices which where joined. The secondary coil was one helix with 3 turns. A cylindrical boundary was chosen, in order to avoid corners generated by rectangles. Air and Copper were the assigned materials. Lastly, the mesh chosen was a *coarse* free tetrahedral mesh (Fig. 5.5).

- **Governing Equations:** The coils were assigned with two different types of excitation for the two physics types:

  a) The *Terminal* feature: The Terminal node provides a boundary condition for connection to external circuits or to a specified voltage. By specifying zero charge, a floating potential condition is obtained. This definition uses the following governing equation:

$$\int_{d\Omega} -n.JdS = I_0 \tag{5.6}$$
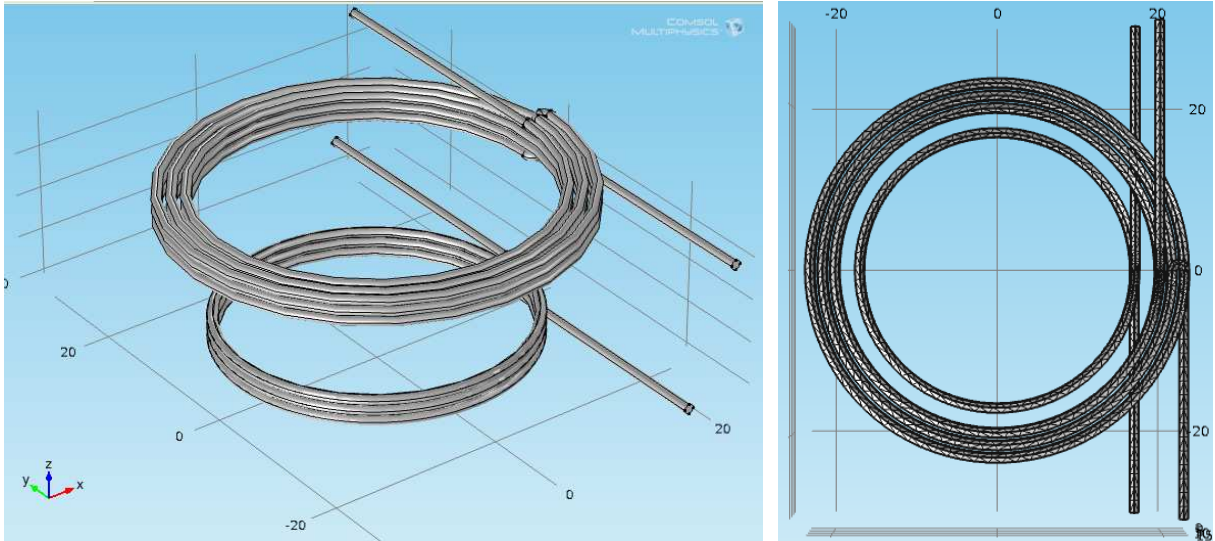
Figure 5.5: 3D coil setup in COMSOL and *coarse* triangular mesh.

One terminal of each coil was assigned with Ground. One terminal of the primary coil was assigned with a current excitation of 1*A*, while one terminal of the secondary coil with 0*A*, in order to calculate the induced voltage in the secondary coil.

(b) The *Edge Current* feature: The Edge Current feature allows us to specify a line current along one or more edges. This definition uses the following governing equations:

$$-n \times H = J_S, \ n \times (H_1 - H_2) = J_S \tag{5.7}$$

The primary and secondary coils were assigned with edge currents of 1*A* and 0*A*.

## 5.3.2    Simulation Results

The model was simulated with the two features. 3D plots were generated for the electric potential and the magnetic flux density, as given in Fig. 5.6. The figures demonstrate how the electric potential and magnetic flux density is maximum around the primary coil. The electric potential is highest at the excited terminal and gradually decreases along the perimeter of the two coils. The magnetic flux linkage between the two coils is also evident from the figure.
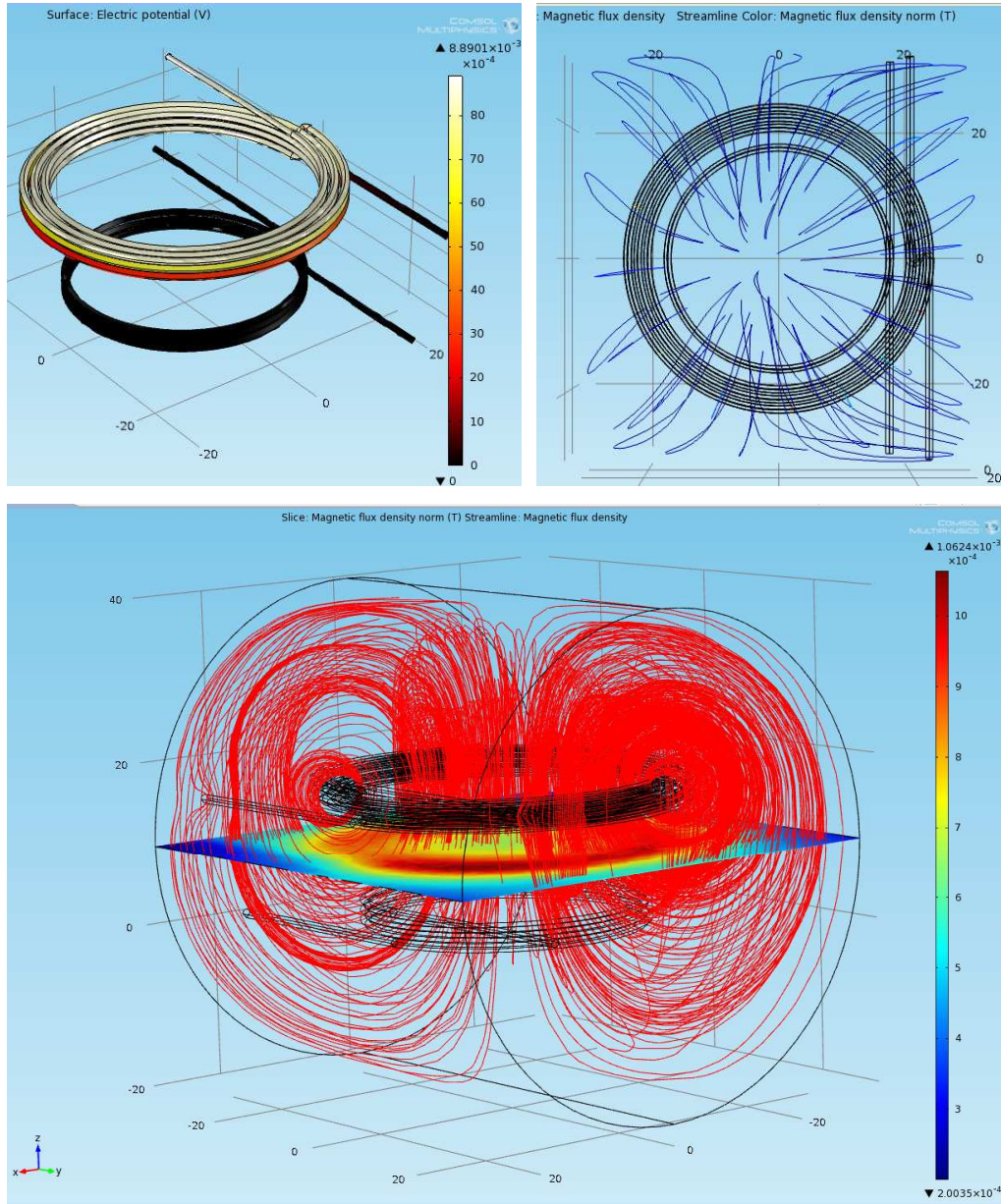
Figure 5.6: Electric potential and magnetic flux density (normal).

### 5.3.3   Inductance Values

The self and mutual inductance of the coils were also found from the 3D simulations. They were conformal with the values calculated by the theoretical analysis. COMSOL finds self–inductance values automatically through its *Global Evaluation* feature in the Results section.

The mutual inductance was found by performing a line integration along the secondary coil

of *tA*, the projection of the magnetic vector potential in the direction of the local tangent vector. The magnetic vector potential components at edges are available as *tAx*, *tAy* and *tAz*, and the edge–tangent vector components are denoted as *t1x*, *t1y* and *t1z*. The projection *tA* is then defined by the dot–product of the tangent vector and the magnetic potential:

$$tA = tAx * t1x + tAy * t1y + tAz * t1z \tag{5.8}$$

The mutual inductance value for the modified coils was found to be $0.33\mu H$ by this method.

### 5.3.4 Parametric Sweep

The mutual inductance has been plotted against four parameters (Fig. 5.7): the radius of the primary coil (the secondary coil radius is kept constant due to implant design constraints), the distance between the two coils, the axial displacement between the two coils, and the angular displacement between the two coils. This is done in order to compare the simulated mutual inductance trends with the results obtained through the equations.

It is demonstrated in Fig. 5.7(a) how the mutual inductance decreases with increasing distance between the two coils, for constant coil sizes. Fig. 5.7(b) shows that a larger primary coil results in a larger mutual inductance. Fig. 5.7(c) and 5.7(d) have a similar trend, which is of decreasing mutual inductance with increasing misalignment of the coils.

The two effects of axial and angular misalignment can be combined, as shown in the previous chapter (Fig. 4.5). Therefore, a similar set of conclusions about the worst–case alignment, such as the ones stated in Section 4.3.2, can be derived with the help of these FEM simulations.

## 5.4 Standards on RF Radiation and Exposure

The IEEE Standards Association mandates standards for safety levels with respect to human exposure to radio frequency electromagnetic fields between the frequencies of $3kHz$ and $300GHz$.

Figure 5.7: (a) Mutual inductance versus coil distance. (b) Mutual inductance versus primary coil radius (coil distance=50*mm*). (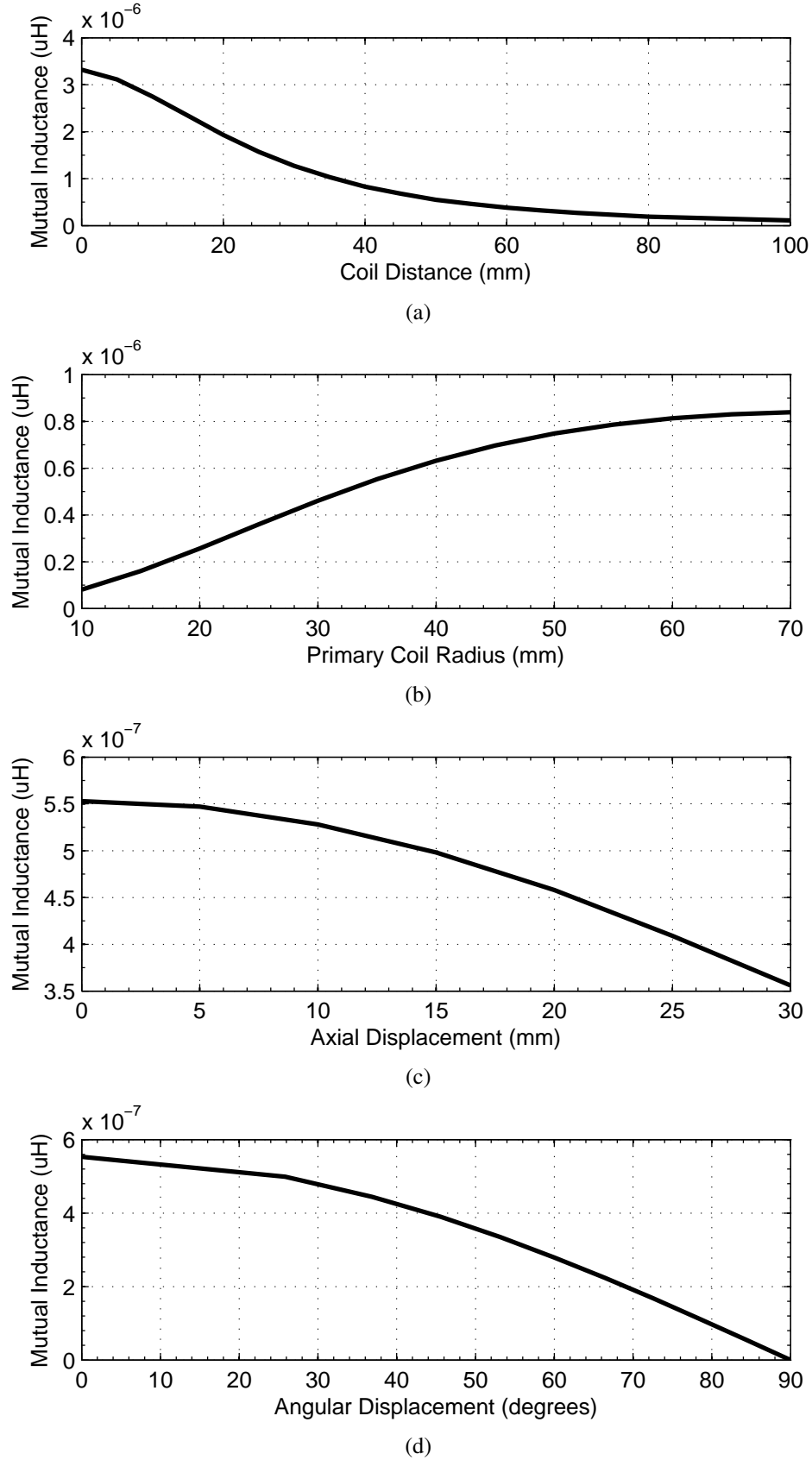c) Mutual inductance versus axial misalignment (coil distance=50*mm*). (d) Mutual inductance versus angular misalignment (coil distance=50*mm*).

These specifications can be safely extended to other living subjects as well. The most recent of these standards is the IEEE Std C95.1™, that has been published in 2005 [51]. In order to implement our power transfer links, it is very important for us to follow these standards and check if the exposure limits are crossed.

Maximum Permissible Exposure (MPE) Limits for controlled RF environments are stated for various frequency sub–ranges. The MPEs are defined in terms of the RMS electric field strength (E) in $V/m$, the RMS magnetic field strength (H) in $A/m$ and the RMS power density (S) in $W/m^2$. The averaging time is 6 minutes. For uniform exposure over the dimensions of the body, for example, certain far–field plane–wave exposures, the exposure field strengths and power densities are compared with the given MPEs. However, for non–uniform exposure such as that in our case, the mean values of the exposure fields, as obtained by spatially averaging the squares of the field strengths or averaging the power densities over an area equivalent to the vertical cross section of the projected area, are compared with the given MPEs [51].

As per our frequencies of interest, we will only talk about two frequency sub–ranges, which are $100kHz$ to $1MHz$, and $1MHz$ to $30MHz$. For both, the RMS electric field strength (E) is $1842/f_M[V/m]$ and the RMS magnetic field strength (H) is $16.3/f_M[A/m]$. Here, $f_M$ denotes the frequency in $MHz$. The RMS power density measure is usually used for higher frequencies.

As can be observed in Fig. 5.2, the maximum RMS E–field is $692/f_M[V/m]$ and the maximum RMS H–field is $7.6/f_M[A/m]$ (converted from Tesla). Both values are lower than the specified MPEs. This proves that for this case for non–uniform exposure, even the maximum field strengths at a certain spatial point are well within the exposure limits, thus eliminating the need for spatially averaging the squares of the field strengths to find its mean value.

## 5.5   EMPro® 3D Electromagnetic Simulations

This section describes the simulations performed by the software EMPro, which is specifically designed for carrying out electromagnetic simulations. It employs two different techniques,
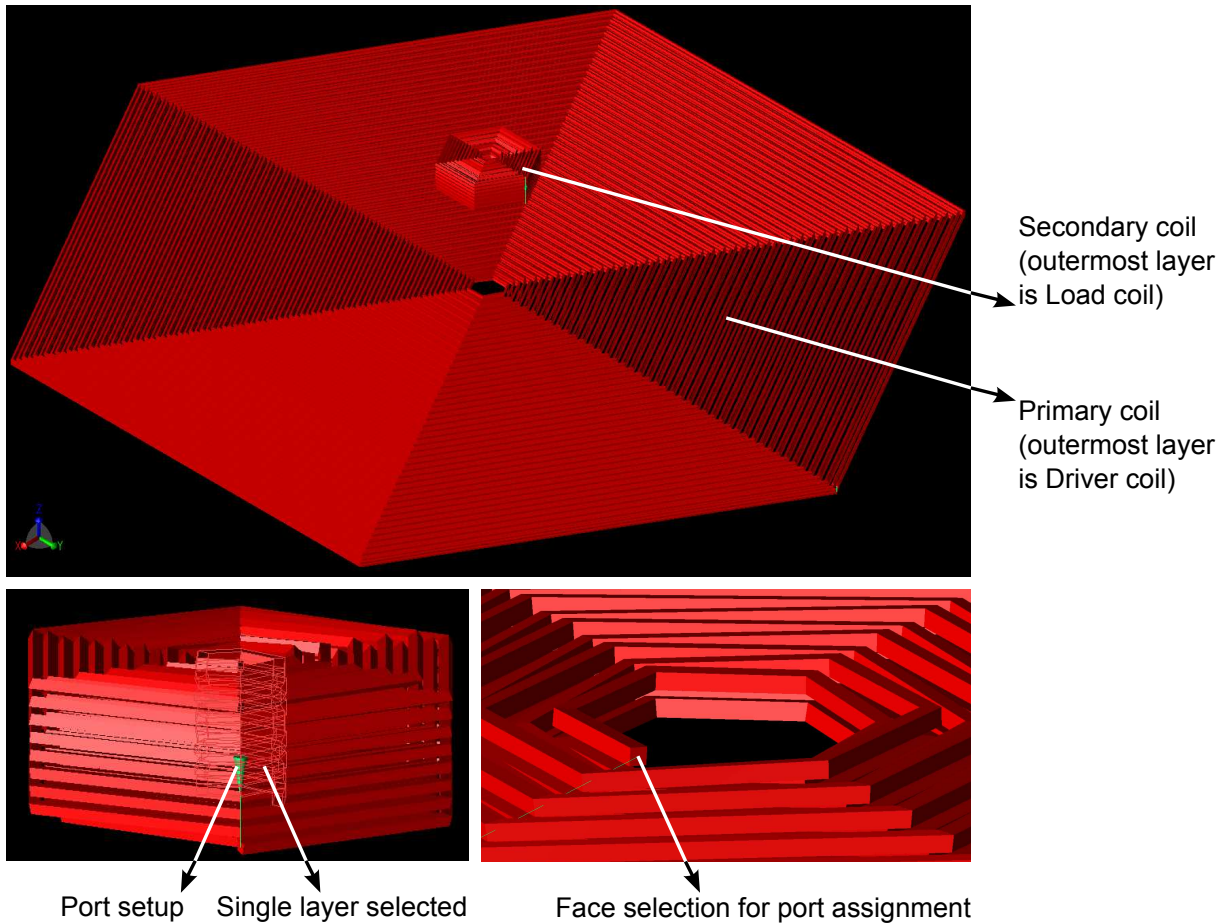
Figure 5.8: 3D coil model in EMPro.

FEM (finite element method) and FDTD (finite–difference time–domain), in order to perform its simulations. FDTD is a time-domain method, whose solutions can cover a wide frequency range with a single simulation run, and treat nonlinear material properties in a natural way. FDTD is preferred when there is a high number of mesh cells, whereas FEM is more efficient for solving high–Q and multi–port applications.

The choice of the technique depends on the kind of model to be simulated. The version of the software used for our simulations is 2011.12. The data collected from the simulations is in the form of scattering parameters (also known as S–parameters), which can be transformed into a number of different electrical parameters such as inductance, resistance and Q–factor.

### 5.5.1   Model and Simulation Setup

The coils are set up in the 3D space using the *helix* geometry feature of the software. Instead of making a circular helix, a hexagonal structure is chosen, which is a very good approximation, and also significantly reduces simulation time. The different layers (helices) of the coils are joined using the *loft faces* feature. The material assigned to the coils is *copper*, and to the rest of the space is *freespace*, with their predefined parameters. The boundary conditions are set as *absorbing* for all the axes (*x*, *y* and *z*).

The excitation for the coils is provided to the ports using a 50*Ohm* voltage source with an amplitude of 1*V* and phase shift of 0°. The ports 1 and 2 are set up as feeds through the start and end faces of the load and driver coils respectively. Fig. 5.8 shows the setup of all the four coils in the 3D model space.

The type of simulation chosen for this model is FEM. We specify the following simulation parameters: adaptive sweep type with 20 sample points, start and end frequencies of 10*kHz* and 10*MHz*, mesh delta error of 0.01 with 10*MHz* refinement frequency, and direct matrix solver with an order of 2 basis functions.

### 5.5.2   Results

Since two ports are assigned to the system of inductor coils, it behaves as a two–port network. The simulations produce S–parameter data, which is a term for defining the network in terms of its incident and reflected *power waves*. The S–parameters are called $S_{11}$, $S_{21}$, $S_{12}$ and $S_{22}$, based on the numbering of the excited ports. They are defined in the following equations:

$$
\begin{aligned}
S_{11} &= \frac{b_1}{a_1} \\
S_{21} &= \frac{b_2}{a_1} \\
S_{12} &= \frac{b_1}{a_2} \\
S_{22} &= \frac{b_2}{a_2}
\end{aligned}
\tag{5.9}
$$
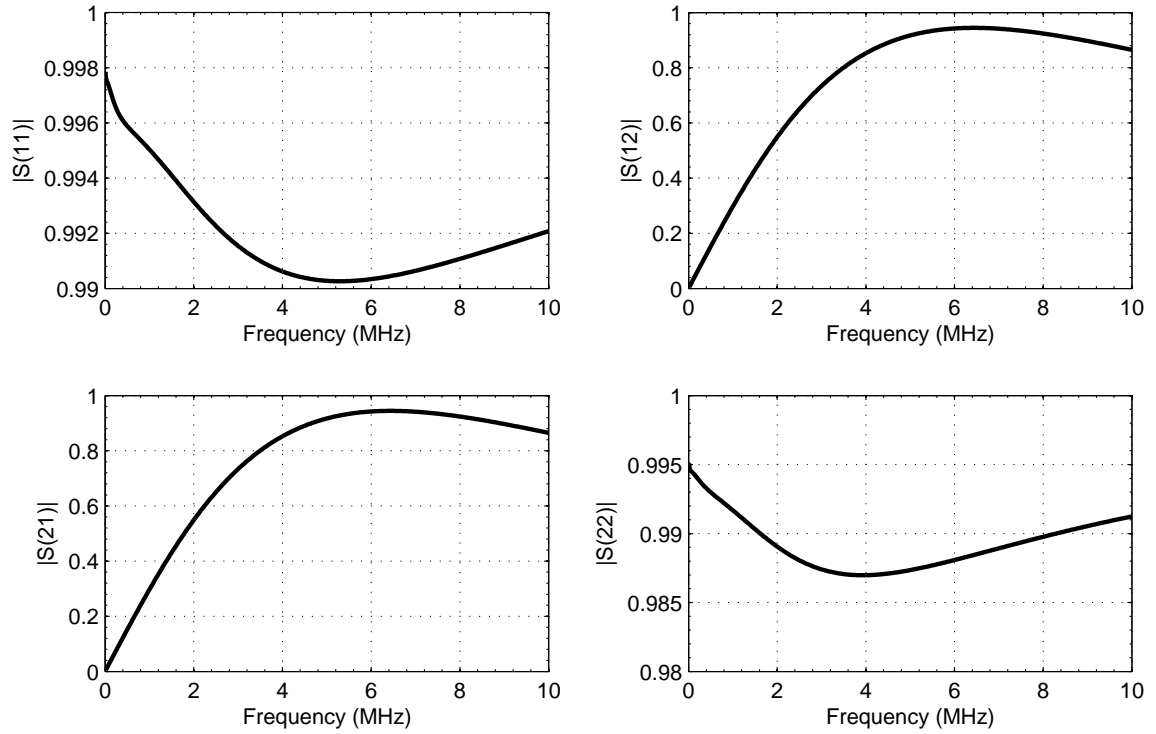
Figure 5.9: Simulated S-parameters of the EMPro model.

where $a_n$ is the incident wave at port $n$ and $b_n$ is the corresponding reflected wave.

The S–parameters can be easily transformed into Z–parameters, which can be used to find values for parameters such as the inductance and the resistance. These equations can be found in several resources on microwave engineering such as [52]. Once the Z–parameter values are found, the following equations are used to find the electrical parameters:

$$L_n = \frac{imag(Z_{nn})}{2\pi f} \tag{5.10}$$

$$M_{mn} = \frac{imag(Z_{mn})}{2\pi f} \tag{5.11}$$

$$R_n = \frac{real(Z_{nn})}{2\pi f} \tag{5.12}$$

where $L_n$, $M_{mn}$ and $R_n$ denote self–inductance, mutual inductance and resistance respectively.

Fig. 5.9 shows the four S–parameter plots that have been simulated for the model within

the given frequency range of 0 to 10$MHz$. As can be observed from the plots, the S–parameters do not have a sharp peak at any particular frequency, which indicates its broad–band nature. The transmission efficiency of the power transfer link can be directly calculated from $S_{21}$ via the following equation:

$$\eta_{21} = 100x|S_{21}|^2[\%] \tag{5.13}$$

By calculating $\eta_{21}$ from the $S_{21}$ data, we achieve transmission efficiencies of approximately 50% and 80% at 2.8$MHz$ and 5$MHz$ respectively, for a coil distance of 50$mm$. The values are comparable with our analytical results but are not accurate with respect to the operating frequencies. This is due to the fact that the coils in the model were made with a plain copper wire structure that has a different equivalent series resistance, instead of the twisted multistrand structure of the Litz wire. The model becomes too complicated for successful computation when Litz wire structures are used. Also, a hexagonal structure was used instead of a perfectly circular helix. The values achieved for the electrical parameters as per equations 5.10, 5.11 and 5.12 were also conformal with the theoretical values with small error margins.

## 5.6   Inclusion of External Structures

The study to observe the behavior of the model with external structures in between and around the external and implant coils is an important one, since it will help predict the efficiency of the power transfer link in the real–life scenario. Therefore, we have conducted a few studies on the impact of external structures in this section. They are listed as follows:

- A *metal plate* with an area of 15x15$cm^2$, made from PEC (Perfect Electric Conductor) from the material library, was inserted between the external and implant coil pairs. This showed a decrease in the transmission efficiency to 27% at 2.8$MHz$.

- A *repeater coil*, with the same configurations as that of the primary coil, was inserted

this time. The distance between the external and implant coils was kept the same, and the repeater was placed at 25*mm* distance from each. The transmission efficiency was observed to increase in this case, to 59% at 2.8*MHz*.

- A material with the properties of *muscle tissue* (of human beings) was used for this simulation. The dielectric properties of permittivity and conductivity at the frequency of interest were taken from [53]. The mass had an area of 50x50*mm*$^2$ and a thickness of 5*mm*, and was placed in the middle of the coil setup.

  As explained in Chapter 2, biological tissue has a low SAR for low–frequency RF signals (below 4*MHz*) and therefore, did not have a very significant impact on the power transmission efficiency. The efficiency reduced to 48% for this simulation, which was a difference of only about 2% with the simulations without the tissue matter.

## 5.7  Summary

This chapter has validated some of the results obtained theoretically with the help of electromagnetic simulations based on Finite Element Method modeling. The two software products used have employed different approaches and techniques to model and simulate the system of four mutually–coupled inductors for optimized wireless power transfer. Both two–dimensional and three–dimensional layouts have been employed to evaluate various physical and electrical parameters of the inductors.

The COMSOL simulations demonstrate quantified electric field and magnetic flux density plots, as well as parameters such as resistance, self and mutual inductance, that successfully validate the theoretical results. Parametric studies have been conducted for mutual inductance versus primary coil size, distance between coils, and their misalignment. Thereafter, the observed trends have been analyzed. Lastly, an eigenfrequency study and comparison with RF exposure limit standards have been performed on the coil model. All of the performed design steps have also been reported sequentially.

The EMPro simulations demonstrate the approach of using S–parameters to calculate vari-ous electrical data of the inductors as well as the overall power transfer efficiency of the system. The results produced match with those achieved through the theoretical analysis. Furthermore, various external components, including biological materials, have been modeled in the system in order to analyze their effects. This has been helpful in order to gather an idea of how such materials will affect the power transfer system in real–life implementations. It is also a good starting point for performing numerical modeling of these effects.

# Chapter 6

# Conclusions

The aim of this thesis was to design and optimize a wireless power transfer link for implementation in bioimplantable telemetry systems. The method of resonance–based inductive coupling has been employed for achieving this goal, and the optimization process has led to the modeling of two power transfer systems based on specific application requirements.

## 6.1  Thesis Contributions

The contributions of this thesis can be outlined as follows:

- Various power transfer links have been reviewed in order to justify the need for a fully–optimized resonance–based inductively–coupled system, that is capable of wirelessly transferring adequate power to small–size low–power biological implants.

- Specific modeling terms involved for fully defining a multilayer helical inductor coil have been introduced and described with equations, with emphasis on the use of Litz wire and its different operating frequencies. With that the power transfer efficiency (PTE) parameter of the system has been analyzed.

- A complete design flow for the inductor modeling and optimization to maximize PTE has been developed. The design and optimization process has been implemented to create

two different inductive coupling systems, namely System 1 and System 2, that operate in the $350 - 850kHz$ and $1.4 - 2.8MHz$ frequency ranges respectively. The efficiencies achieved for the two systems are 77.13% and 80.66% respectively at a coil distance of $50mm$. Other parameters of both systems have also been tabulated. Conclusions have been made on observed trends of the inductors' physical and electrical parameters.

- A power transfer circuit that uses the designed inductors has been developed and circuit specifications have been described. Relationships for input and output power with other electrical parameters have been defined in order to simplify the process of maximizing the power delivered to the load (PDL).

  Maximized PDL values of $22.3dBm$ and $0.76dBm$ have been achieved for System 1 and System 2 respectively. Furthermore, a novel relationship has been developed between the number of turns in the primary coil and placement of the peak power with respect to coil distance.

- A power harvesting circuit using discrete components, that uses a rectifier and a voltage regulator, has been demonstrated, which is capable of delivering an output power of $420mW$. Also, a charge pump capable of producing an output voltage of $26V$ with an $8.08V$ input voltage has been developed for the power harvester.

  A typical application system where the inductive power transfer system can be implemented has been demonstrated, with descriptions of the RF transceiver, the microcontroller, the IC level power harvester and the interface electronics. The size of the implant is comparable to devices that can be placed inside the chest cavity of a rabbit for obtaining physiological data from the heart with the help of bio–sensors.

- The issue of axial and angular misalignment between the primary and secondary coils has been analyzed, with an account on the different equations available. The functions involved in calculating misalignment in terms of the coupling coefficient $k$, using MATLAB® codes, have been sequentially outlined.

Modeling of the worst–case distance and alignment that is still capable of delivering adequate power to the implant in [43] has been performed.

- Finite element method (FEM) electromagnetic modeling of the coils has been performed using COMSOL® and EMPro® software, using both 2D and 3D models. The results are in accordance to the theoretical results from the previous chapters and verify their validity, with a maximum error of only 5.6%. The FEM simulations also check the models against RF safety regulations and demonstrate the effects of external elements on the power transfer link.

All of the individual contributions make up the modeling sequence of the entire power transfer system, starting from the design of the four individual inductors and the power transfer circuit, to misalignment issues and FEM modeling. This will equip future system designers with a step–by–step procedure manual for designing such power transfer links.

## 6.2   Comparison with Previous Works

Our work is compared against some similar endeavors undertaken in this field, as summarized in Table 6.1. It can be observed that the power transfer efficiency achieved in this work is the highest with respect to coil distance and implant coil size.

Table 6.1: Comparison of this research with other similar works

| AREAS | Cong [1] | Kurs [14] | Jow [16] | RamRakhyani [17] | This Work |
|---|---|---|---|---|---|
| Coupling Type | Inductive | Resonance–based | Inductive | Resonance–based | Resonance–based |
| Inductor Type | Helical | Helical | Printed Spiral | Multilayer Helix | Multilayer Helix |
| Circuit Type | Integrated | Discrete | Discrete | Discrete | Discrete |
| Implant Coil Size | 2.5$mm$ radius 1$mm$ height | 30$cm$ radius 20$cm$ height | 10$mm$ radius – | 11$mm$ radius 2.5$mm$ height | 7.5$mm$ radius 4.5$mm$ height |
| Efficiency | *No Data* | 40% at 7*radius | 30% at 2*radius | 82% at 2*radius | 81% at 7*radius |
| Optimization | No | No | Yes | Yes | Yes |
| Misalignment | No | No | No | No | Yes |

## 6.3 Future Work

Based on the achievements of this thesis, there is some scope for future developments to be made on the work done, which will increase its completeness. They are listed as follows:

- Conducting further simulations in the FEM electromagnetic front, in order to include all the parameters involved in the modeling and optimization process of the inductors. This will also provide a way of easily manipulating the structures, and changing their orientation and environment in order to draw better conclusions on the various effects on the power transfer link.

- Manufacturing of prototypes for the inductors, the power transfer circuit and the power harvesting unit, and integrating them with the prototype implant already available that uses battery as a power source. This will enable measurements of real–life data, observations on inaccuracy and suggestions on possible improvements.

- Miniaturization of the implant as well as the inductor from a discrete off–chip component to an integrated on–chip component such as a printed spiral coil (PSC). This will help make the the size of the implant comparable to devices that can be placed *in–vivo* smaller living subjects like the rat or the genetically–engineered mouse.

- Extension of the results achieved to a Helmholtz configuration in order to increase the total power delivered to the load. Also, analyses can be performed for other coil links such as the two–coil link, three–coil link, and repeaters in between the external and the implant coils. However, this will require extensive modifications to be made to the modeling equations and the circuit theory used.

# Bibliography

[1] Peng Cong, N. Chaimanonart, W.H. Ko, and D.J. Young. A Wireless and Battery-less 130mg 300uW 10b Implantable Blood-Pressure-Sensing Microsystem for Real-Time Genetically Engineered Mice Monitoring. In *Solid-State Circuits Conference - Digest of Technical Papers, 2009. ISSCC 2009. IEEE International*, pages 428–429,429a, feb. 2009.

[2] W.A. Van Gool, H.F. Pronker, M. Mirmiran, and H.B. Uylings. Effect of Housing in an Enriched Environment on the Size of the Cerebral Cortex in Young and Old Rats. *Experimental Neurology*, 96(1):225–232, 1987.

[3] William C. Brown. History of Power Transmission by Radio Waves. *IEEE Transactions on Microwave Theory and Techniques*, MTT-32(9):1230–1242, 1984.

[4] R. Stuart Mackay. Radio Telemetering from Within the Human Body. *IRE Transactions on Medical Electronics*, ME-6(2):100–105, 1959.

[5] J. Nagumo, A. Uchiyama, S. Kimoto, T. Watanuki, M. Hori, K. Suma, A. Ouchi, M. Kumano, and H. Watanabe. Echo Capsule for Medical Use (A Batteryless Endoradiosonde). *IRE Transactions on Bio-Medical Electronics*, 9(3):195–199, 1962.

[6] Xiaoyu Liu, Fei Zhang, S.A. Hackworth, R.J. Sclabassi, and Mingui Sun. Wireless Power Transfer System Design for Implanted and Worn Devices. In *Bioengineering Conference, 2009 IEEE 35th Annual Northeast*, pages 1 –2, april 2009.

[7] S.C. Malpas, M. Lim, D. McCormick, R. Kirton, B. Van Vliet, A. Easteal, C. Barrett, S. Guild, and D. Budgett. A Novel Implantable Blood Pressure Telemetry Device: Comparison between Data Sciences and Telemetry Research Systems. *FASEB Journal*, 22:738.7, 2008.

[8] B. Warneke and K.S. Atwood, B. Pister. Preliminary Smart Dust Mote. *Hot Chips*, 12(1), 2000.

[9] W.J. Heetderks. RF Powering of Millimeter- and Submillimeter-Sized Neural Prosthetic Implants. *IEEE Transactions on Biomedical Engineering*, 35(5):323–327, 1988.

[10] K. Finkenzeller. *RFID Handbook*. Wiley, London, U.K., 2003.

[11] P.R. Troyk. Injectable Electronic Identification, Monitoring, and Stimulation Systems. *Annual Review on Biomedical Engineering*, 1:177–209, 1999.

[12] J.W. Throff, W. Hort, and H. Lichti. Diameter of Coronary Arteries in 36 Species of Mammalian from Mouse to Giraffe. *Basic Research in Cardiology*, 79(2):199–206, 1984.

[13] D. Russell, D. McCormick, A. Taberner, P. Nielsen, P. Hu, D. Budgett, M. Lim, and S. Malpas. Wireless Power Delivery System for Mouse Telemeter. In *Biomedical Circuits and Systems Conference, 2009. BioCAS 2009. IEEE*, pages 273–276, nov. 2009.

[14] André Kurs, Aristeidis Karalis, Robert Moffatt, J. D. Joannopoulos, Peter Fisher, and Marin Soljačić. Wireless Power Transfer via Strongly Coupled Magnetic Resonances. *Science*, 317(5834):83–86, 2007.

[15] H.A. Haus and W. Huang. Coupled-Mode Theory. *IEEE Proceedings*, 79(10):1505–1518, 1991.

[16] Uei-ming Jow and Maysam Ghovanloo. Design and Optimization of Printed Spiral Coils for Efficient Transcutaneous Inductive Power Transmission. *IEEE Transactions on Biomedical Circuits and Systems*, 1(3):193–202, 2008.

[17] A.K. RamRakhyani, S. Mirabbasi, and M. Chiao. Design and Optimization of Resonance-Based Efficient Wireless Power Delivery Systems for Biomedical Implants. *Biomedical Circuits and Systems, IEEE Transactions on*, 5(1):48–63, 2011.

[18] Mehdi Kiani, Uei-ming Jow, and Maysam Ghovanloo. Design and Optimization of a 3-Coil Inductive Link for Efficient Wireless Power Transmission. *IEEE Transactions on Circuits and Systems*, 5(6):579–591, 2011.

[19] Meysam Zargham and P Glenn Gulak. Maximum Achievable Efficiency in Near-Field Coupled Power-Transfer Systems. *IEEE Transactions on Circuits and Systems*, 6(3):228–245, 2012.

[20] S.I. Babic and C. Akyel. Calculating Mutual Inductance Between Circular Coils With Inclined Axes in Air. *IEEE Transactions on Magnetics*, 44(7):1743–1750, 2008.

[21] Milton Abramowitz and Irene A. Stegun. *Handbook of Mathematical Functions with Formulas, Graphs, and Mathematical Tables*. Dover, New York, ninth dover printing, tenth gpo printing edition, 1964.

[22] K. Bong, E. Levi, Z. Zabar, and L. Birenbaum. Mutual Inductance of Noncoaxial Circular Coils with Constant Current Density. *IEEE Transactions on Magnetics*, 33(5):4303–4309, 1997.

[23] Reid R Harrison. Designing Efficient Inductive Power Links for Implantable Devices. In *IEEE International Symposium on Circuits and Systems, 2007*, pages 2080–2083, may 2007.

[24] C.M. Zierhofer and E.S. Hochmair. Geometric Approach for Coupling Enhancement of Magnetically Coupled Coils. *IEEE Transactions on Biomedical Engineering*, 43(7):708–714, 1996.

[25] Suresh Atluri and Maysam Ghovanloo. Design of a Wideband Power-Efficient Inductive Wireless Link for Implantable Biomedical Devices Using Multiple Carriers. In *2nd International IEEE EMBS Conference on Neural Engineering, 2005*, pages v–ix, march 2005.

[26] Gabriele Grandi, Marian K Kazimierczuk, Senior Member, Antonio Massarini, and Ugo Reggiani. Stray Capacitances of Single-Layer Solenoid Air-Core Inductors. *IEEE Transactions on Industry Applications*, 35(5):1162–1168, 1999.

[27] Qin Yu and Thomas W Holmes. A Study on Stray Capacitance Modeling of Inductors by Using the Finite Element Method. *IEEE Transactions on Electromagnetic Compatibility*, 43(1):88–93, 2001.

[28] Zhi Yang, Wentai Liu, and Eric Basham. Inductor Modeling in Wireless Links for Implantable Electronics. *IEEE Transactions on Magnetics*, 43(10):3851–3860, oct. 2007.

[29] M.W. Baker and R. Sarpeshkar. Feedback Analysis and Design of RF Power Links for Low-Power Bionic Systems. *IEEE Transactions on Biomedical Circuits and Systems*, 1(1):28–38, march 2007.

[30] C. D. Sijoy and S. Chaturvedi. Calculation of Accurate Resistance and Inductance for Complex Magnetic Coils Using the Finite-Difference Time-Domain Technique for Electromagnetics. *IEEE Transactions on Plasma Science*, 36(1):70–79, 2008.

[31] G. S. Dimitrakakis, E. C. Tatakis, and E. J. Rikos. A New Model for the Determination of Copper Losses in Transformer Windings with Arbitrary Conductor Distribution under High Frequency Sinusoidal Excitation. In *European Conference on Power Electronics and Applications, 2007*, pages 1–10, sep. 2002.

[32] New England Wire Technologies. Litz Wire - Technical Information - technical.pdf [Online]. Available: http://www.newenglandwire.com/litz.asp. Accessed: 2012.

[33] A. Massarini, M.K. Kazimierczuk, and G. Grandi. Lumped Parameter Models for Single- and Multiple-Layer Inductors. In *27th Annual IEEE Power Electronics Specialists Conference*, volume 1, pages 295–301, jun 1996.

[34] Wikipedia. Litz Wire [Online]. Available: http://en.wikipedia.org/wiki/Litz-wire. Accessed: 2012.

[35] F. Tourkhani and Viarouge P. Accurate Analytical Model of Winding Losses in Round Litz Wire Windings. *IEEE Transactions on Magnetics*, 37(1):538–543, 2001.

[36] Massimo Bartoli, Nicola Noferi, and Alberto Reatti. Modeling Litz-Wire Winding Losses in High-Frequency Power Inductors. In *27th Annual IEEE Power Electronics Specialists Conference*, pages 1690–1696, 1996.

[37] Anil Kumar Ramrakhyani and Gianluca Lazzi. On the Design of Efficient Multi-Coil Telemetry System for Biomedical Implants. *IEEE Transactions on Biomedical Circuits and Systems*, pages 1–13, 2012.

[38] S. Senjuti, K. Fricke, A. Dounavis, and R. Sobot. Misalignment Analysis of Resonance-Based Wireless Power Transfer to Biomedical Implants. In *IEEE Canadian Conference on Electrical and Computer Engineering, 2012. CCECE 2012*, may 2012.

[39] S. Senjuti and R. Sobot. Inductor Modeling for Implantable Wireless Power Delivery Systems. In *IEEE International Conference for Upcoming Engineers, 2012. ICUE 2012*, aug. 2012.

[40] Aristeidis Karalis, J.D. Joannopoulos, and Marin Soljačić. Efficient Wireless Non-Radiative Mid-Range Energy Transfer. *Annals of Physics*, 323(1):34 –48, 2008.

[41] Mehdi Kiani and Maysam Ghovanloo. The Circuit Theory behind Coupled-Mode Magnetic Resonance-Based Wireless Power Transmission. *IEEE Transactions on Circuits and Systems*, 59(8):1–10, 2012.

[42] James C. Lin. A New IEEE Standard for Safety Levels with Respect to Human Exposure to Radio-Frequency Radiation. *IEEE Antennas and Propagation Magazine*, 48(1):157–159, 2006.

[43] L. Luo, K. De Gannes, K. Fricke, S. Senjuti, and R. Sobot. Low-Power CMOS Voltage Regulator Architecture for Implantable RF Circuits. In *Fourth International EURASIP Workshop on RFID Technology*, pages 99–106, sep. 2012.

[44] John F. Dickson. On-chip High-Voltage Generation in NMOS Integrated Circuits Using an Improved Voltage Multiplier Technique. *IEEE Transactions on Solid-State Circuits*, 11(6):374–378, 1976.

[45] Maysam Ghovanloo and Suresh Alturi. A Wide-Band Power-Efficient Inductive Wireless Link for Implantable Microelectronic Devices Using Multiple Carriers. *IEEE Transactions on Circuits and Systems*, 54(10):2211–2221, 2007.

[46] F. W. Grover. *Inductance Calculations*. Dover, New York, 1964.

[47] S.I. Babic, C. Akyel, and M.-M. Mahmoudi. Mutual Inductance Calculation for Non-Coaxial Circular Air Coils with Parallel Axes. *Progress In Electromagnetics Research*, 91:287–301, 2009.

[48] Wikipedia. Helmholtz Coil [Online]. Available: http://en.wikipedia.org/wiki/Helmholtz-coil. Accessed: 2013.

[49] Wikipedia. Finite Element Method [Online]. Available: http://en.wikipedia.org/wiki/Finite-element-method. Accessed: 2013.

[50] M. N. O. Sadiku. *Numerical Techniques in Electromagnetics*. CRC Press, Florida, 2001.

[51] IEEE International Committee on Electromagnetic Safety (SCC39). IEEE Standard for Safety Levels with Respect to Human Exposure to Radio Frequency Electromagnetic Fields, $3kHz$ to $300GHz$, IEEE Std C95.1, 2005.

[52]  D. M. Pozar. *Microwave Engineering*. Wiley, Toronto, Canada, 1998.

[53]  S Gabriel, R W Lau, and C Gabriel.  The Dielectric Properties of Biological Tissues: II. Measurements in the Frequency Range 10*Hz* to 20*GHz*. *Physics in Medicine and Biology*, 41:2251–2269, 1996.

# Curriculum Vitae

| | |
|---|---|
| **Name:** | Shawon Senjuti |
| **Post-Secondary Education and Degrees:** | Queen Mary, University of London<br>London, United Kingdom<br>2006 - 2009 B.Eng. |
| | The University of Western Ontario<br>London, ON, Canada<br>2010 - 2013 M.E.Sc. |
| **Honors and Awards:** | Ontario Graduate Scholarship (OGS)<br>2012-2013 |
| **Related Work Experience:** | Teaching Assistant 2010 - 2013<br>The University of Western Ontario |

**Publications:**

- S. Senjuti, K. Fricke, A. Dounavis and R. Sobot. Misalignment Analysis of Resonance–Based Wireless Power Transfer to Biomedical Implants. IEEE Canadian Conference on Electrical and Computer Engineering 2012, Montreal, Canada.

- S. Senjuti and R. Sobot. Inductor Modeling for Implantable Wireless Power Delivery Systems. IEEE Int'l Conference for Upcoming Engineers 2012, Toronto, Canada.

- L. Luo, K. De Gannes, K. Fricke, S. Senjuti and R. Sobot. Low–Power CMOS Voltage Regulator Architecture for Implantable RF Circuits. IEEE Int'l EURASIP Workshop on RFID Technology 2012, Torino, Italy.